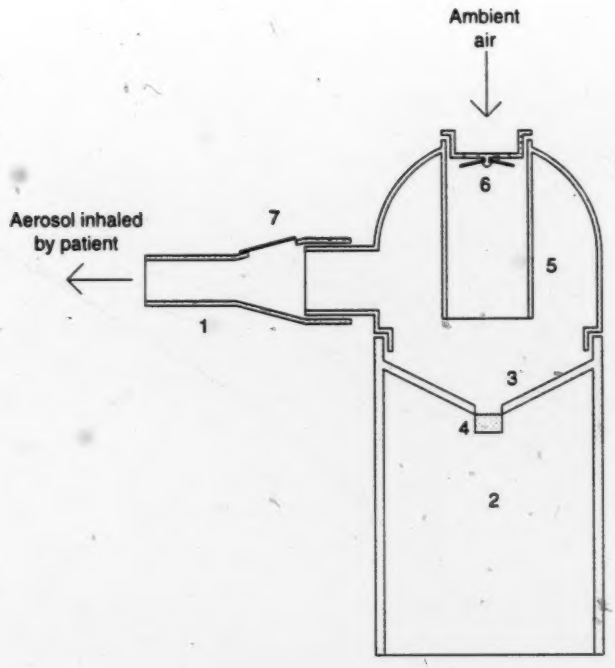

Figure 3.3. A schematic of an ultrasonic nebulizer (2) and attached mouthpiece (1) shown during inhalation. The nebulizer includes the reservoir (3), pizo-electric crystal (4) and baffles (5). Here, when the patient inhales, air is drawn through the inlet valve (6). During exhalation, the inlet valve (6) closes, and air is expelled through the exhalation valve (7). The electronics for the piezo-electric crystal are not shown.

increase, decrease, or remain constant with increasing flow rate (Knoch & Wunderlich, 1994). During exhalation, aerosol is still produced by the vented nebulizer and exits at a rate equal to the mass flow rate of the compressor air. The volumetric flow rate out of a vented jet nebulizer is therefore unsteady, and dependent on the breathing parameters of the patient.

Ultrasonic nebulizers do not use a compressed air source to produce the aerosol droplets. Instead, vibrations in the reservoir solution caused by a submerged piezo-electric crystal produce instabilities in the fluid that cause droplets to be formed (Mercer, 1981). Often, a series of one-way valves directs inhaled air through the nebulizer bowl as

in a vented jet nebulizer, and directs exhaled air through a vent in the mouthpiece. However, during exhalation, there is often no air flow through the nebulizer, but aerosol is still produced. This aerosol collects in the dome of the nebulizer, so that when the patient begins the inhalation maneuver, the number density of aerosol droplets is initially very high, but then drops to a lower level for the remainder of the inhalation cycle.

3.3 Determining solution concentration within aerosol droplets output by nebulizers

The output characteristics of jet and ultrasonic nebulizers, such as aerosol size distribution, nebulizer solution temperature and concentration, and nebulization rate, have been reviewed in the literature (for example, Mercer *et al.* 1968, Mercer 1981, Clay *et al.* 1983, Sterk *et al.* 1984, Phipps & Gonda 1990, Smye *et al.* 1992, and Langford & Allen 1993). Statistical models of nebulizer performance have also been presented (Smye *et al.* 1991). However, the solution concentration of the aerosol droplets is not readily measured directly, but can be calculated from other measurements. The methodology to calculate the concentration of solute within aerosol droplets will first be described for unvented jet nebulizers producing an aerosol from an aqueous solution. Modifications to this procedure in order to adapt it for vented jet and ultrasonic nebulizers will then be discussed. Modifications to this methodology to include drugs formulated as suspensions is currently being investigated, and is not included here.

3.3.1 Theory

Consider a control volume surrounding an unvented jet nebulizer (Figure 3.4). Conservation of mass indicates that during a given time period, t, the change in mass of the solution in the nebulizer is given by:

$$\Delta m_{neb} = m_{out} - m_{in} \tag{3.1}$$

where m_{neb} is the mass of solution in the nebulizer, m_{in} is the mass of water vapor entering the nebulizer during time t, and m_{out} is the total mass leaving the nebulizer during time t and is given by:

$$m_{out} = m_s + m_l + m_v \tag{3.2}$$

where m_s is the mass lost as solute, m_l, is the mass lost as liquid water, and m_v is the mass lost as water vapor. By determining m_s, and m_l, the average solution concentration of the droplets over the time period t can be calculated. Note that the mass rate of air entering the nebulizer equals the mass rate of air leaving the nebulizer, and therefore, assuming that it does not interact chemically with the water or solutes, it does not appear in Equation (3.2).

In Equation (3.1), the change in total mass of solution in the nebulizer, Δm_{neb}, is easily measured by weighing the nebulizer before and after the time period t. The mass of water vapor entering the nebulizer, m_{in}, can be calculated knowing the temperature and relative humidity of the ambient air with the equation:

$$m_{in} = c_{w,in} \cdot Q \cdot t \tag{3.3}$$

where Q is the volume flow rate of air entering the nebulizer, and $c_{w,in}$ is the water vapor concentration in this air. The concentration of water vapor c_w is given by the

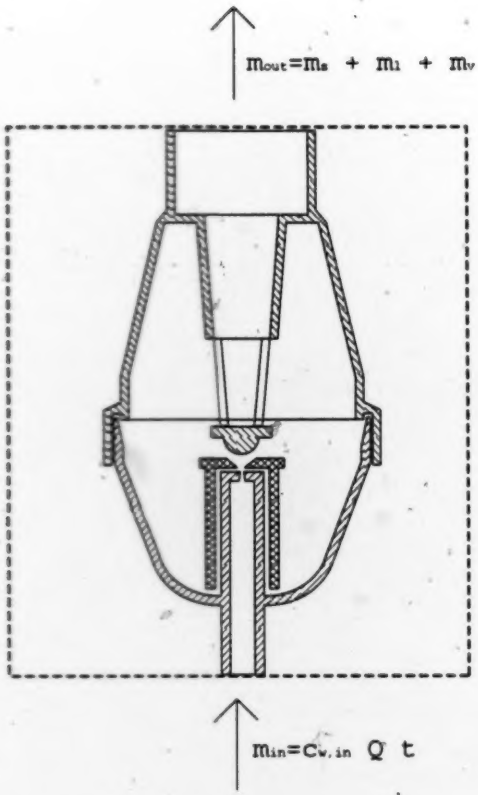

Figure 3.4. A schematic of the control volume around a jet nebulizer.

Antoine equation (Reid, Prausnitz, & Sherwood, 1977):

$$c_w = RH \cdot 363.8 \cdot \exp\left(\frac{-4943}{273.15 + T_a}\right) \tag{3.4}$$

where T_a is the air temperature in degrees Celsius, RH is the relative humidity of the air ($RH < 1.0$), and c_w is given in g/cm^3. To calculate $c_{w,in}$, the temperature and relative humidity of the ambient air entering the nebulizer are used in Equation (3.4).

The mass of solids leaving the nebulizer, m_s, in equation (3.2) can be measured by collecting the aerosol droplets on a filter, then drying the filter and weighing the collected solids. The mass leaving the nebulizer as water vapor, m_v, is calculated in a

similar way to m_{in}, but using the dry bulb temperature of the aerosol leaving the nebulizer. Alternatively, m_s can be calculated by measuring the amount of solute remaining in the nebulizer from the concentration and mass of the reservoir solution at the end of each minute. Any solute not present in the reservoir solution will have left the nebulizer in droplets.

Equations (3.1) and (3.2) can now be solved for m_l, and the average solution concentration in the droplets c_{avg} is then given by:

$$c_{avg} = \frac{m_s}{\left(\frac{m_s + m_l}{\rho}\right)} \tag{3.5}$$

where ρ is the density of the solution, and is given by (Ferron, 1977):

$$\rho = \frac{m_w + m_s}{m_w + \left(\frac{m_s}{\rho_s}\right)} \tag{3.6}$$

where ρ_s is the density of the solid. It is assumed that the density of the solution is independent of the solution concentration to allow equations (3.1) - (3.5) to be solved without an iterative method. This assumption will be justified in Section 3.3.2.2.

The final piece of information that is required to calculate the solution concentration in the droplets is the relative humidity of the air leaving the nebulizer, so that the value of m_v can be calculated. However, the air output by medical nebulizers typically has a relative humidity of greater than 95% (often greater than 99%), and standard measurement techniques do not have sufficient accuracy in this range. Measurements are further complicated by the presence of the droplets. Fortunately, as will be shown later, the droplets leaving the nebulizer are in equilibrium with the

surrounding air, and this allows us to accurately predict the relative humidity of the output air.

Aerosols output by medical nebulizers are typically polydisperse, with geometric standard deviations ranging from approximately 1.5 - 2.0, indicating that these aerosols have a wide range of particle sizes. Evaporation rates and stabilization times for hygroscopic droplets are strongly dependent on droplet size (Ferron & Soderholm, 1990), with smaller droplets having higher evaporation rates and shorter stabilization times. Thus, the smaller droplets may have a different concentration from the larger droplets. However, droplets greater than 1 μm in diameter will all have the same concentration if they are in equilibrium with their environment. To see this, consider that an aerosol droplet in equilibrium with its environment satisfies the following equilibrium condition (Morrow, 1986):

$$RH = C_K \cdot C_R \tag{3.7}$$

where RH is the relative humidity of the surrounding air, C_K is the Kelvin correction for surface curvature, and C_R is the vapor pressure reduction due to dissolved solids (Raoult's Law for an ideal solution, or an expression for a non-ideal solution such as Cinkotai (1971) for NaCl). For droplets greater than approximately 1 μm in size, the Kelvin correction causes changes in the droplet size of less than 0.1% and can be neglected (Morrow, 1986). Thus, since there is no dependence on droplet diameter in C_R, the solution concentration in all droplets greater than approximately 1 μm in diameter will be the same if the aerosol is in equilibrium with its environment.

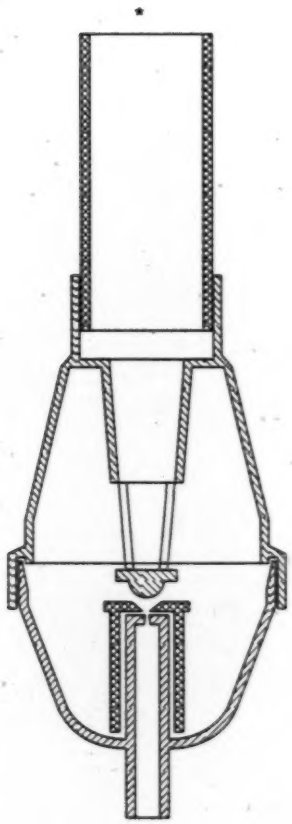

Figure 3.5. A schematic of a vented jet nebulizer with a length of tube attached vertically for measuring the equilibrium condition of the aerosol leaving the nebulizer. The asterisk marks the approximate measuring point.

3.3.2 Experimental Validation

3.3.2.1 Droplet Equilibrium

Before the above methodology can be applied to a nebulizer, it must be verified that droplets leaving the nebulizer are in equilibrium with the surrounding environment. The output distributions of three DeVilbiss Pulmo-Neb® disposable nebulizers (DeVilbiss Health Care (Canada) Inc., Barrie, ON, Canada) delivering normal saline (0.9% NaCl)

were measured using a phase Doppler anemometer, or PDA (Dantec Electronics Inc., Mahwah, NJ, USA), with 4 different lengths of plastic tubes (5 cm, 10 cm, 25 cm, and 40 cm in length, inside diameter 2.54 cm) attached vertically to the opening of the nebulizer (Figure 3.5). The tubes were attached vertically to minimize deposition of the aerosol due to gravitational settling (the settling velocity of the droplets considered here is at least an order of magnitude smaller than the fluid velocity, so sedimentation is not expected to influence the distribution significantly). Ambient laboratory conditions during the data collection were 23.0±0.2 °C, and 34.0±2.5% relative humidity measured by a calibrated thermometer and a hygrometer (Fisher Scientific, Mississauga, ON) respectively. The flow rate through the nebulizer was measured at 6.6±0.1 litres/min by water displacement. At this flow rate, the 40 cm extension gives the aerosol approximately 2 seconds of transit time beyond the nebulizer exit before its exposure to ambient conditions.

Each nebulizer was first measured without an extension, then with each extension added. This procedure was repeated 10 times for each nebulizer to obtain a statistical measure of the nebulizer performance. Figure 3.6 shows the difference between the average diameter of the droplets measured without an extension and the diameter of the droplets measured with each of the extensions added. The dotted lines indicate the 4% measurement error of the phase Doppler anemometer. As can be seen in Figure 3.6, the measured average diameter of the droplets does not change significantly as the extra lengths of tubes are added to the exit of the nebulizer. Additionally, a statistical comparison showed no significant difference between the measurements (Student's *t*-test,

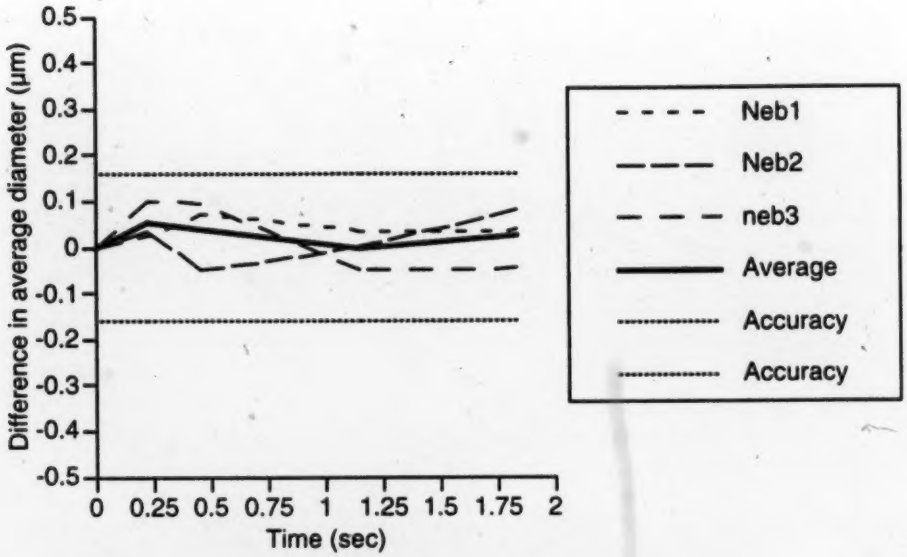

Figure 3.6. The change in average diameter of droplets with time after leaving the nebulizer, and before interacting with the ambient air. The dotted lines indicate the measurement error of the phase Doppler anemometer (4%)

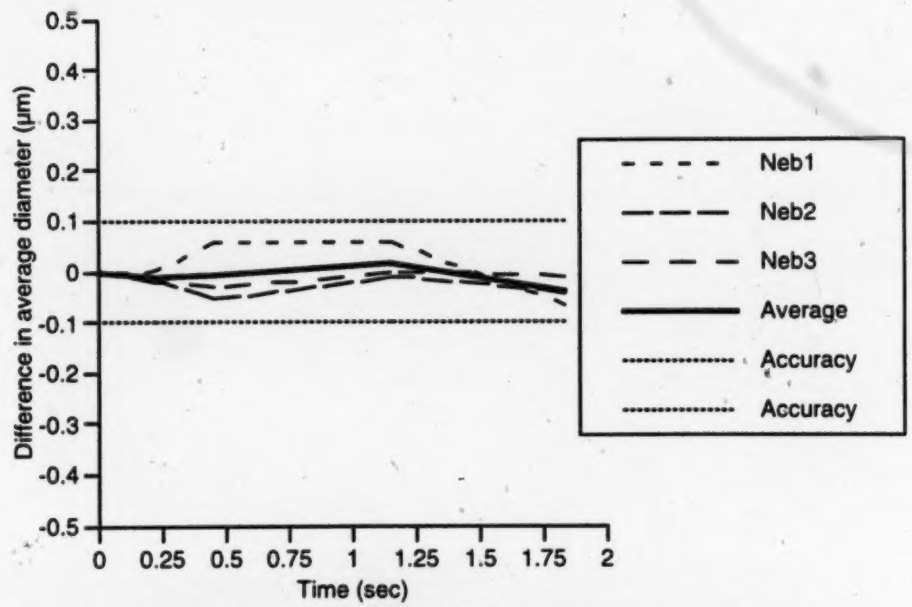

Figure 3.7. The change in average GSD of the droplet distribution with time after leaving the nebulizer, and before interacting with the ambient air. The dotted lines indicate the measurement error of the phase Doppler anemometer (4%)

$P > 0.1$). From this we can conclude that the average size of the droplets is not changing as they traverse the length of the extensions.

It has been shown (Ferron & Soderholm, 1990) that smaller droplets have a much faster stabilization time than larger droplets. This may manifest itself as a change in the distribution, without a significant change in the average diameter. To check this, similar tests to those performed on the average droplet diameter were performed with the geometric standard deviation (GSD) of the aerosol. Figure 3.7 shows the variation of the GSD of the droplet distribution with the addition of different lengths of tubes, and the measurement error of the PDA system. Again, both the graph, as well as statistical tests (F test, $P>0.1$) indicate that there is no significant change in the GSD of the aerosol distribution.

Ferron & Soderholm (1990) estimate that the time required for a *single* pure water droplet with a size equal to the mass median diameter (MMD) of the droplet distribution measured here (on average, about 8 μm for these three nebulizers) to reach equilibrium with 99.5% air is approximately 20 seconds. Approximately the same time is required for a single solid salt particle to absorb water and become isotonic. This seems to indicate that the droplets may not be in equilibrium when they exit the nebulizer, and that the time allowed for the droplets to stabilize in this experiment is too short. However, Eisner *et al.* (1990) considered the stabilization time of aerosol clouds similar to those measured here at the exit of the nebulizer, including the effect of two-way coupling between the phases (see section 2.5.2 for more details) and predict stabilization times of only a few tenths of seconds. By considering aerosol clouds and the ability of the droplets to affect the relative humidity of the surrounding air, the amount of water that

must evaporate/condense from each droplet is small, and thus the length of time needed for the system to come into equilibrium is short. Additionally, if >99% of the droplets are returned to the reservoir then the droplet number concentration may be up to 2 orders of magnitude greater inside the nebulizer than in the aerosol exiting the nebulizer. This will have the effect of further reducing the amount of water from each droplet that must evaporate to humidify the air in the nebulizer, and further reduce the length of time required for the aerosol to come into equilibrium.

Recently, Ferron *et al.* (1997) calculated the hygrosocpic growth of droplets through three nebulizers using the hygroscopic growth model of Ferron & Soderholm (1990) with a simple correction for the relative humidity of the air surrounding the droplets and found that more than 97% of any droplet growth happened in the first 0.1 seconds, which is approximately the average residence time of a droplet in the tested nebulizers. In the case of the PulmoNeb studied here, Ferron *et al.* show very little growth of the droplets from the point of creation to the exit of the nebulizer, and little change in the concentration in the droplets, which supports the conclusions drawn here. However, Ferron *et al.* also suggest that this is only the case with the PulmoNeb, and not a general conclusion for all nebulizers.

If this last suggestion is true, then the method described here would not be useful. However, Ferron *et al.* also predict large changes in the MMD and GSD of the aerosol during the next 3 seconds of the aerosol's existence. These large changes should be measurable using the technique described above, but are not observed in any of three different nebulizer models studied here. Ferron *et al.* do not present experimental evidence to support their conclusions. Additionally, calculations with the two-way

coupled model presented in Section 2 indicate that the droplets are in equilibrium upon exiting the nebulizer. These issues are addressed in more detail in Section 3.5.

Based on the theoretical considerations and experimental evidence, we can conclude that the droplets are in equilibrium as they exit the nebulizer. Further, from the discussion of Equation (3.7), we know that for all droplets with diameters greater than approximately 1 μm, the solution concentration in the droplets will be the same.

3.3.2.2 Droplet Solution

The methodology to measure the solution concentration described above is applied to the same model of nebulizer discussed above (DeVilbiss Pulmo-Neb® disposable nebulizer) driven by the same compressor (DeVilbiss Pulmo-Aide® compressor) and delivering two unit dose nebules (a total of 5 ml of solution). Each Ventolin® nebule (DIN 00897345, Glaxo Canada Inc., Mississauga, ON, Canada) contains 2.5 mg of salbutamol sulfate dissolved in 2.5 ml of normal saline (0.9% NaCl). Ambient laboratory conditions during data collection were 23.0±0.2 °C, and 25.0±2.5% relative humidity. The flow rate through the nebulizer was measured as 6.6±0.1 l/min. A random sample of nebulizers from the same manufacturing lot was used to give a statistical sample of performance.

To calculate the concentration of the droplet solution, a nebulizer was weighed after the addition of the two Ventolin® nebules, then run for one minute, during which all droplets exiting the nebulizer were collected on a filter (Watman EPM2000) that collects 99.997% of particles >0.3 μm (Figure 3.8). At the end of the minute, the nebulizer was reweighed, and a 50 μl sample of the remaining nebulizer solution was removed to

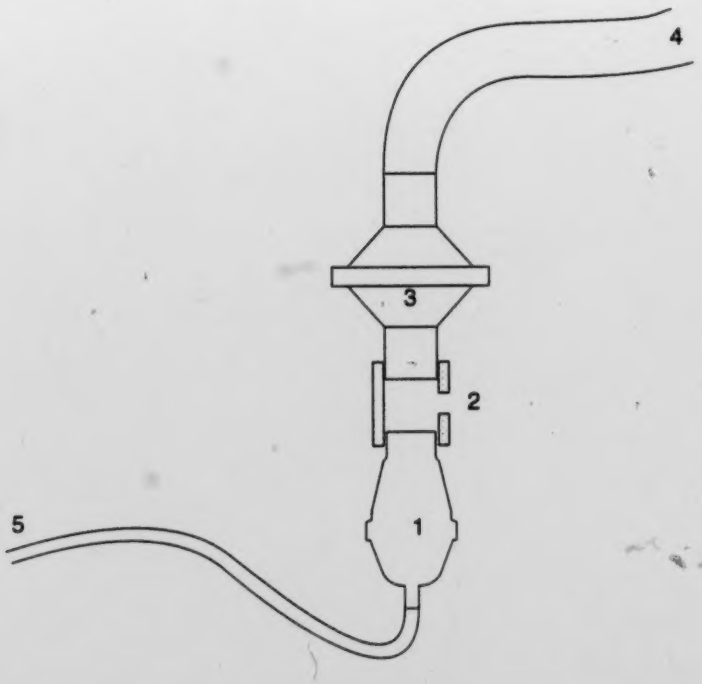

Figure 3.8. A schematic of the experimental setup to collect the solids output by a nebulizer. The nebulizer (1) is attached to the filter (3) via a short section of tube (2) with holes to allow ambient air to be entrained to match the flow rate of the vacuum pump. The compressor and vacuum pump are attached to the test apparatus via hosing (5) and (4) respectively

measure the solute concentration by freezing point osmometry (model 5004, Precision Systems Inc., Natick, Mass., USA).

For the second minute, the nebulizer was first weighed, then run for a minute, during which time the droplets were again collected on a filter. The nebulizer was weighed again, and another sample of the nebulizer solution was removed and its concentration measured. This procedure was repeated until the nebulizer began to operate intermittently. The results of these measurements are shown in Table 3.1. Data was not collected while the nebulizer operated intermittently. When the nebulizer is not running continuously, there is no droplet production, and no evaporation from the

Minute	Δm_{neb} (g)	m_s (mg)	Concentration (mg/ml)
1	0.302±0.004	2.15±0.08	10.21±0.4
2	0.282±0.007	2.10±0.06	10.26±0.03
3	0.267±0.006	2.03±0.07	10.41±.04
4	0.278±0.004	2.18±0.03	10.61±0.05
5	0.276±0.002	2.18±0.01	10.79±0.07
6	0.259±0.005	2.05±0.06	11.01±0.04
7	0.265±0.002	2.20±0.02	11.28±0.04

Table 3.1. Total mass Δm_{neb} leaving the nebulizer during each minute, the mass of solids m_s collected on the filter during each minute, and the measured concentration of the solute in the nebulizer solution at the end of each minute, for an initial volume of 5.0 ml in the nebulizer. All values are mean ± standard error.

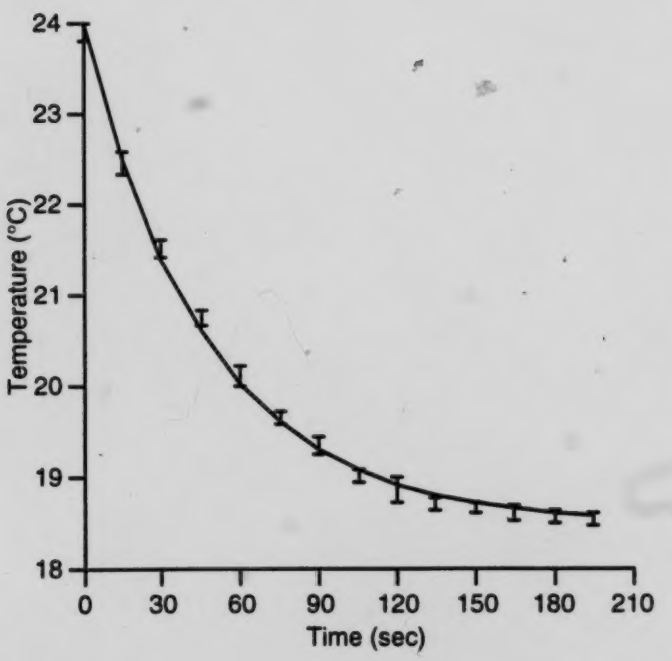

Figure 3.9. Plot of the temperature of the air exiting the nebulizer as a function of time (points with error bars) and Equation 3.8).

droplets, so the output water vapor content is no longer a simple function of time (c.f. Equation 3.9).

The temperature of the air leaving the nebulizer was measured with a thermocouple in the jet exiting the nebulizer and protected from droplet impaction by a small plastic shield, and was found to have an exponential character. Figure 3.9 shows the measured data and the function:

$$T_a = 18.5 + 5.5 \cdot \exp(-1.29 \cdot t) \tag{3.8}$$

where t is the time in minutes. This equation is substituted into the Antoine equation (Equation 3.4) to give an equation for the output concentration of water vapor, $c_{w,out}$, as a function of time. The output relative humidity of medical nebulizers delivering isotonic solutions has been estimated as greater than 99% (Ferron & Gebhart, 1988). Since we have found that the droplets are in equilibrium upon exiting the nebulizer, we can use Equation (3.8) to give us the relative humidity of the air exiting the nebulizer.

If the droplets exiting the nebulizer have a solution concentration equal to the initial concentration of the nebules (i.e. 0.9% NaCl, and 1 mg/ml salbutamol sulfate), the equilibrium relative humidity would be 99.48%. For a solution 10% greater than the initial concentration of the nebules, the equilibrium relative humidity would be 99.41%. Thus,the change in solution concentration during nebulization has little effect on the output relative humidity, and a constant output relative humidity of 99.4% is assumed here to allow Equations (3.1) - (3.5) to be solved without an iterative method. Substituting Equation (3.8) into Equation (3.4) with a relative humidity of 99.4% gives:

$$c_{w,out} = 361.6 \cdot \exp\left(\frac{-4943}{291.65 + 5.5 \cdot \exp(-1.29 \cdot t)}\right) \tag{3.9}$$

Equation (3.9) is then multiplied by the flow rate of air out of the nebulizer to convert the units to g/sec, and integrated numerically to give the total amount of water vapor leaving the nebulizer in a given time period.

Integrating Equation (3.9) with the present data, the amount of water leaving the nebulizer as vapor during the first minute of operation is 0.124±0.002 g, so that from Table 3.2 and Equations (3.1) and (3.2) we find the amount of solution leaving the nebulizer is $m_l + m_s = 0.212 \pm 0.005$ g. The average concentration of the solution in the droplets is then calculated by equation (3.5)

$$c_{sp} = \frac{0.00215 \pm 0.00008}{\left(\frac{0.212 \pm 0.005}{1.004}\right)} = 0.0102 \pm 0.0004 \frac{g}{ml} \qquad (3.10)$$

Values for the other minutes of nebulizer operation are given in Table 3.2. In each minute, the average solution concentration within the droplets is within 2% of the concentration measured in the nebulizer solution at the end of the minute.

If the droplets are evaporating slightly to humidify the air in the nebulizer, then the concentration of the solution in the droplet can be expected to increase slightly as it moves from the point at which it was formed at the venturi, to the point at which it comes into equilibrium with the surrounding air. Therefore, at any given point in time, the concentration of solution in the droplets will be slightly different (in fact, slightly higher) than the concentration of the solution in the nebulizer reservoir, but the two concentrations will remain close, and they both will increase at approximately the same rate. This is seen in the above results in which the droplet solution concentration *averaged* over each minuteis equal to the measured nebulizer reservoir solution concentration at the *end* of each minute.

Minute	Calculated average droplet concentration (mg/ml)	Measured nebulizer solution concentration (mg/ml)
1	10.2±0.4	10.21±0.04
2	10.2±0.5	10.26±0.03
3	10.4±0.5	10.41±.04
4	10.5±0.4	10.61±0.05
5	10.6±0.2	10.79±0.07
6	10.9±0.4	11.01±0.04
7	11.3±0.3	11.28±0.04

Table 3.2. The calculated average concentration of the solution in the droplets over one minute of nebulizer operation compared to the concentration of the nebulizer solution measured at the end of the minute for an initial concentration of the nebulizer solution of 10.0 mg/ml (1.0 mg/ml salbutamol sulfate, and 9.0 mg/ml NaCl). All values are mean ± standard error.

Start Time (min.)	End Time (min.)	Averaging interval (min.)	Average Droplet Concentration (mg/ml)
0	7	7	10.6±0.1
1	7	6	10.7±0.1
2	7	5	10.8±0.1
3	7	4	10.9±0.1
4	7	3	11.0±0.17
5	7	2	11.1±0.2
6	7	1	11.3±0.3

Table 3.3. The calculated average concentration of the droplets produced by the nebulizer when averaging over different time intervals with Equation (3.5) from the data in Table (3.1). The measured concentration of the nebulizer reservoir solution at the end of the 7th minute of operation was 11.28±0.04 mg/ml.

Because the concentration is increasing over the nebulization period, the average solution concentration calculated with Equation (3.5) will depend on the time interval over which the averaging occurs. To investigate this, the concentration increase in the droplets is calculated from the data in Table (3.1) using time intervals from 1 to 7 minutes. It can be seen from the results in Tables (3.1) and (3.3) that measuring the concentration of the nebulizer reservoir solution at the end of each minute gives the best estimate of the average solution concentration in the droplets.

In a clinical setting, nebulizers are typically operated when there is not enough solution in the reservoir to continuously produce aerosol (i.e. the nebulizer operates intermittently or 'sputters'). It is therefore important to consider how the above results might be extrapolated to predict the concentration of the solution in the droplets produced when the nebulizer is sputtering. When the nebulizer is sputtering, the operation of the nebulizer is characterized by short periods where the nebulizer is running 'continuously', and periods when the nebulizer is not producing droplets. It has been reported by several authors (Mercer *et al.*, 1968, O'Callaghan *et al*,. 1989, Langford & Allen, 1993) that during the final period of the nebulization session, there was minimal drug output, but continued vapour water output by the nebulizers these authors tested. This is consistent with the loss of water directly from the nebulizer reservoir by evaporation during the periods when the nebulizer is not producing droplets. To account for this in the calculations, m_v in Equation (3.2) must include water losses due to this evaporation, or Equation (3.5) will underestimate the calculated average concentration in the droplets.

More important to calculations here is the effect that any evaporative losses during sputtering would have on the ability of the measurement of the nebulizer reservoir

solution concentration at the end of a minute to predict the average concentration of the droplets produced during that minute. It is reasonable to expect that any increase in concentration of the nebulizer reservoir solution when the nebulizer is not producing droplets will be at a rate equal to or lower than when the nebulizer is producing droplets, since the surface area available for evaporation is lower when the nebulizer is not producing droplets.

The evaporation rates of four PulmoNeb nebulizers were measured by blocking the flow of reservoir solution to the venturi to stop droplet production, and running the nebulizers for one hour. On average, 0.7818±0.0034 g (mean ± standard error) of liquid was lost over the hour, giving a rate of 0.0132 ± 0.0001 g/min. of liquid evaporating from the nebulizer solution, less than 5% of the rate of mass loss during droplet production. No solute was lost from the reservoir solution during the test period.

Estimating the effect that this evaporative loss will have on the calculated average solution concentration in the droplets is difficult since it is highly dependent on the performance of the nebulizer, and the length of time during which the nebulizer 'sputters'. Most studies of nebulizer performance end the nebulization session when there is a pause of 15 - 20 seconds in droplet output. We have chosen a pause of 15 seconds in the droplet output to signify the end of the nebulization session. Using this criterion, the PulmoNeb nebulizer sputters for less than 3 minutes before the nebulization session is stopped , and the total amount of time during the nebulization session that each PulmoNeb nebulizer did not produce droplets was between 1 minute, and 1 minute 15 seconds.

If we now consider an entire nebulization session that ends when there is a 15 second pause in droplet production, then the concentration of the reservoir solution at the end of each minute will accurately predict the average solution concentration in the droplets over the 1 minute time interval during the first part of the session when the nebulizer is continuously producing droplets. Near the end of the session when the nebulizer starts to sputter, the concentration of the reservoir solution may underestimate the average solution concentration in the droplets by up to 5-6% by the end of the nebulization session. The magnitude of this error will depend strongly on the performance of the nebulizer tested, particularly if the nebulizer sputters for a long time. However, it has been noted that most of the nebulizers tested in this lab sputter for shorter periods than the PulmoNeb, so the error can be expected to be less than the 5-6% estimated for the PulmoNeb.

3.3.3 Application to Vented Jet and Ultrasonic Nebulizers

The primary operational difference between normal jet and vented jet nebulizers is that on inhalation the patient draws air through the bowl of the nebulizer. This means that m_{in} in Equation (3.1) (the mass of water vapor entering the nebulizer during the time period t) is now the sum of the water vapor entering from the compressed air source and from the vent. Theoretically, m_{in} can be easily calculated from Equation (3.3) with Q equal to the inhalation flow rate of the patient. Then the rest of the theory is directly applicable to vented jet nebulizers.

However, this is not a practical method because the fluctuating flow rate through the droplet producing region of the nebulizer during the breathing cycle makes integration

of the mass losses by water vapour difficult. Here, for vented jet nebulizers, we assume that the concentration in the droplets is constant over the entire nebulization session. If the droplets are in equilibrium with the surrounding air, they can be collected during simulated tidal breathing on a Respiragard II filter (Marquest Medical Products Inc. Englewood, CO) placed between the nebulizer mouthpiece and the breathing simulator (see Figure 3.12) and their mass determined. (Because the droplets are in equilibrium with the surrounding air, they will not evaporate after depositing on the filter as the air passes through the filter from the simulated tidal breathing. The validity of this assumption was checked by additionally collecting the exhaled droplets, and accounting for all the mass of the system within 2%.) To determine the mass of solids collected on the filter, the filter was dried, treated with 5 ml of water, sonicated for 30 minutes, and the concentration of the remaining solution determined by freezing point osmometry (Precision Systems Inc., Natick MA). The average solution concentration was then determined by dividing the mass of solute by the total mass of liquids collected on the filter.

As with the unvented jet nebulizers, it is assumed that the droplets are in equilibrium with the surrounding air when they exit the mouthpiece of the nebulizer. To test this, a Pari LCJet+ nebulizer was driven by the same DeVilbiss Pulmo-Aide compressor as the unvented jet nebulizer tested above with a dry compressed air source (0% RH) line attached to the inlet vent on the nebulizer. Dry air was pumped though the nebulizer at 48 l/min, so that the flow rate of air exiting the nebulizer was 54 l/min (800 cm^3/s), which is approximately equal to tidal breathing during light exercise (Rudolf *et al.* 1990).

The same lengths of tubes used with the unvented jet nebulizer considered previously were added to the exit of the vented nebulizer to allow up to 2 additional seconds for the droplets to come into equilibrium with the surrounding air. It was again found that there was no significant difference in the average size of the measurements (Student's t test, $P > 0.1$) or in the GSD (F test, $P > 0.1$) indicating that as for the unvented jet nebulizer, the droplets are in equilibrium with the surrounding air when they leave the nebulizer. In this experiment, dry air from a compressed air line was used instead of ambient air from the room to supply air to the nebulizer. If air from the room was used (e.g. RH = 34%), the droplets need to evaporate less to humidify the air, and they would come into equilibrium faster. The conclusion drawn from the experiment is unchanged.

The methodology presented in Section 3.3.2 was also adapted for a DeVilbiss Aerosonic® (Model 5000) ultrasonic nebulizer delivering single dose nebules of Ventolin® by Prokop *et al.* (1995a) who showed that the droplets are in equilibrium when they exit the nebulizer, although two distinct intervals in each breathing cycle can be identified by their differing MMDs and particle number concentration. Prokop *et al.* then modified Equations (3.1) - (3.5) to account for the noted variation in MMD and number density of the aerosol throughout the inhalation cycle. The reader is referred to Prokop *et al.* (1995a) for a detailed description of the modifications.

3.3.4 Calculation of Reservoir Solution Concentration for Unvented Jet Nebulizers

The above procedure for calculating the average concentration in droplets output by unvented jet nebulizers requires that a sample of the nebulizer reservoir solution be

extracted each minute. For a nebulizer that has a long run time, or for a nebulizer that has a very small volume of liquid in the reservoir at the end of the nebulization period, the extraction of this sample could significantly impact the measured performance of the nebulizer. In the above tests, this was avoided by using large volume fills, so the small amount of liquid extracted for concentration was not a significant portion of the total reservoir volume. However, when characterizing the output of nebulizers used in a clinical setting, it is important to use the volume fills typically used in clinical settings to correctly estimate the clinical performance. In this case, the procedure described above for calculating the solution concentration in the droplets may itself impact the results. To avoid these complications, a method of predicting the reservoir solution concentration during the nebulization session from a single measurement of the reservoir solution concentration at the end of the nebulization session is needed.

The concentration of solution in the reservoir of a nebulizer at time t is given by (Mercer, 1981):

$$\frac{c(t)}{c_0} = \left(\frac{V_0}{V_0 - (A+W)Q \cdot t} \right)^{\frac{W}{A+W}} \tag{3.11}$$

where c = solute concentration at time t
c_0 = initial solute concentration
V_0 = initial volume of liquid in the nebulizer
A = volume of droplets leaving the nebulizer per unit volume of air
W = volume of water vapor leaving the nebulizer per unit volume of air
Q = air flow rate through the nebulizer

The factor $V_0 - (A+W)Q \cdot t$, is simply the residual volume of the reservoir solution at time t and can be easily measured by weighing the nebulizer. As can be seen in Figure 3.10, the agreement between the measured values of the reservoir solution concentration and the values predicted by Equation (3.11) are excellent.

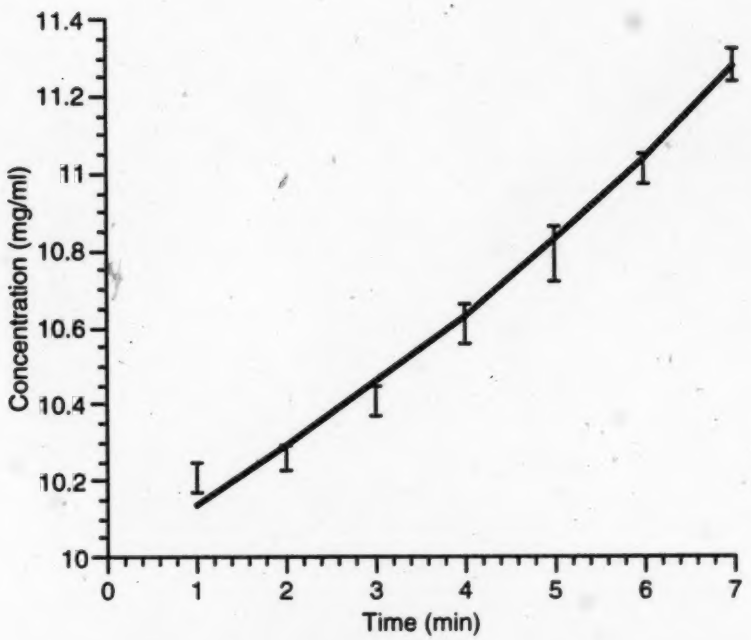

Figure 3.10. Measured concentration of the reservoirs solution for 8 PulmoNeb disposable nebulizers given in Table 3.1 and the values predicted by Equation (3.11). Error bars indicate standard error of the measurements.

3.3.5 Miscellaneous issues

There are a number of issues that need to be addressed before a nebulizer can be tested with this methodology. First, it must be determined if the droplets are in equilibrium with the surrounding air when they exit the nebulizer using the procedure described in Section 3.3. If the droplets are not in equilibrium when they exit the nebulizer, then this methodology is not directly applicable.

To characterize the output of the nebulizer accurately, the size distribution, and the number of droplets per second exiting the nebulizer are required. Since the PDA system used here only measures the droplets over a small measuring volume (typically

10^{-3} mm^3) the size distribution of the entire output must be determined from values measured at a series of locations.

To determine the number of such measurement locations required, the variation of nebulizer output across the nebulizer opening was investigated by measuring the droplet size distribution at 2 mm intervals across the exit of a PulmoNeb nebulizer without a mouthpiece (inside diameter of exit tube =18.7 mm). The measured distributions were tested for similarity using the same procedure used in Section 3.3.2.1 to determine if the droplets are in equilibrium when they exit the nebulizer. No significant change was found in the MMD or GSD of the droplet distribution as the measuring volume was moved across the interior of the opening. However, when the measuring volume was directly over the edge of the opening, there was a slight decrease in the measured MMD, which may be due to shrinkage of droplets caused by the entrainment of ambient air by the plume exiting the nebulizer. Additionally, the number of droplets counted by the PDA varied monotonically by approximately 16% over the nebulizer opening, with the minimum recorded when most of the aerosol cloud was between the measuring volume and the sensing optics. This may be due to rescattering of the refracted light by other droplets, since rotating the nebulizer had no effect on the results.

As long as the measuring point was inside the opening of the nebulizer, and the measuring point was no more than 0.5 cm from the top of the opening, the measurement of the MMD and GSD of the droplet distribution was found to be independent of the location of the measuring volume with respect to the opening of the nebulizer. The measuring point was chosen to be as close to the center of the opening and to the top of the nebulizer as possible to minimize any possible droplet shrinkage from the entrainment

of ambient air. Correction for the droplets not counted due to the optical depth of the cloud was done by a mass balance, and will be described in Section 3.4.1.1.

The humidity and temperature of the air available to the compressor were controlled by placing the compressor in a chamber, described by Prokop *et al.* (1995b), in which dried air was mixed with saturated air to obtain a continuous supply of air of 50% RH, and 23°C. Temperature and relative humidity were measured with a thermometer and hygrometer (Fisher Scientific, Ottawa, ON) respectively, placed in the chamber.

3.4 Calculation of Regional Dosage

We now possess the tools to predict the regional dosage delivered from a nebulizer to different parts of the lung. The first step in this procedure requires a series of bench-top measurements that characterize the output of the nebulizer. Next, this information is input into a computer program which first processes the data into a form usable by the deposition model described in the previous chapter. The computer program then uses the deposition model to calculate the probability of the aerosol droplets depositing in different generations of a Weibel 'A' lung scaled to a total lung capacity of 3000 cm^3. Finally, the program converts the deposition probabilities to regional dosages for the extrathoracic, bronchial, and alveolar regions of the lung, and outputs the results. This section describes which measurements are taken on the bench, and overviews how the computer program calculates the regional dosages from the given data. A flowchart of the program is given in Figure 3.11, and the data files are listed in Appendix A (input files) and Appendix B (output files).

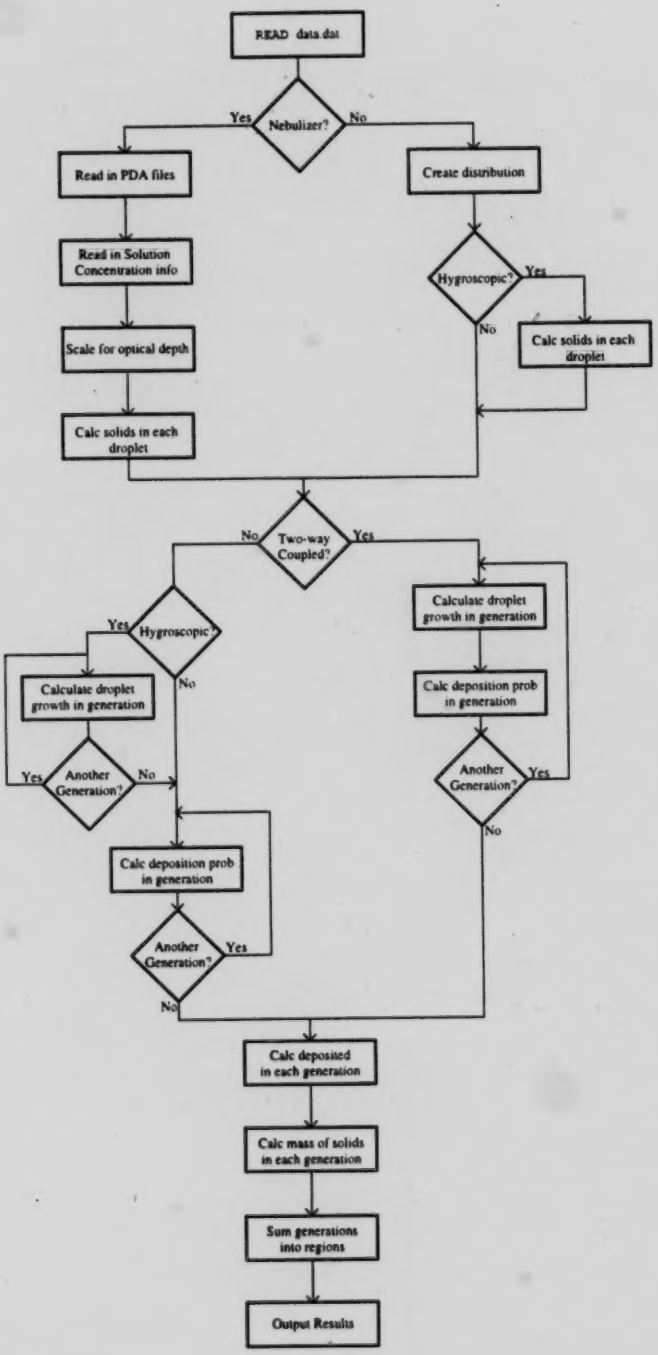

Figure 3.11. A flowchart for the program to calculate the dosage delivered to different regions of the respiratory tract.

As an example of an unvented jet nebulizer, this methodology will be applied to the Hudson T Updraft II nebulizer (Model 1732, Hudson RCI, Temecula, CA) driven by a DeVilbiss Pulmo-Aide compressor delivering a single unit dose nebule of Ventolin®. The modifications to the procedure needed to predict the regional dosage from a vented jet nebulizer will also be discussed. Primarily, these modifications are in the bench measurements and the preprocessing of the data, since the hygroscopic growth calculations, the calculation of the deposition probabilities, and the calculation of the dosages are the same. As an example of a vented jet nebulizer, this methodology will be applied to a Pari LCJet+ nebulizer (Pari GmbH, Starnberg, Germany) driven by the same compressor, and delivering the same drug. Modifications necessary for predicting the regional dosages from one particular ultrasonic nebulizer were discussed by Prokop *et al.* (1995a), and the reader is referred there for details.

3.4.1.1 Unvented Jet Nebulizers

Six Hudson T Updraft II nebulizers were tested to give a statistical sample of nebulizer performance. The nebulizer was weighed before and after the addition of the solution to be nebulized. The nebulizer was then run for 1 minute using the compressor in the controlled humidity and temperature chamber, during which time the droplet distribution was measured with the PDA. At the end of the minute, the nebulizer was re-weighed. This constitutes the data for the first minute of nebulizer operation. The second minute of data was collected by running the nebulizer for an additional minute, during which time a measurement if the size distribution was taken with the PDA. The nebulizer was then reweighed at the end of the minute. This procedure was repeated until there was a period of 15 seconds occurred during which no droplets were produced by the

Data Minute	Nebulized Mass (g)	Concentration (mg/ml)
1	0.189±0.024	
2	0.193±0.025	
3	0.197±0.025	
4	0.206±0.015	
5	0.189±0.011	
6	0.182±0.012	
7	0.177±0.019	
8	0.146±0.021	
9	0.117±0.022	
10	0.090±0.022	
11	0.079±0.017	1.23±0.04
Total	1.76±0.07 (70.4%)	

Table 3.4. Total mass leaving the nebulizer during each minute, and the final concentration of solids (salbutamol sulfate and NaCl) in the nebulizer solution at the end of the nebulization period. All values are mean ± standard error. The value in parentheses indicates the nebulized mass as a percentage of the initial mass of solution in the nebulizer

nebulizer. At the end of the nebulization session, the nebulizer was weighed a final time, and a sample of the reservoir solution was removed for concentration assay.

Table 3.4 gives average results of the measurements just described. The droplet size distribution was essentially lognormal with a mass median diameter (MMD) of 5.57±0.16 μm and a geometric standard deviation (GSD) of 1.95±0.10. The average run time for the nebulizers was 10.6±0.2 minutes, and is rounded up to 11 minutes for presentation purposes.

Many of the parameters commonly used to characterize the performance of nebulizers can be calculated from this data. For example, the efficiency of the nebulizer is defined as the amount of drug that leaves the nebulizer as an aerosol divided by the initial amount of drug in the nebulizer, and can be calculated to be 63.6% here (using the average values). If the size distribution is assumed to be perfectly log normal, then the respirable fraction (fraction of mass contained in droplets between 1 μm and 6 μm) can be calculated to be 0.56. The delivered respirable fraction is defined as the product of the efficiency and the respirable fraction, and can be calculated to be 35.5%.

Cipolla *et al.* studied the performance of the T-Updraft II for delivering RhdNase and found a similar respirable fraction of 50.5%, a lower efficiency of 46.4%, yielding a delivered respirable fraction of 23.4%. Additionally, Loffert *et al.* (1994) studied the T-Updraft II and measured an efficiency of 64.8% and a delivered fraction of 40.1%. No respirable fraction is reported, but a value of approximately 62% can be inferred.

However, these performance measures may not provide an accurate representation of the ability of the nebulizer to deliver drug to the respiratory tract as the hygroscopic nature of the droplets is not accounted for, and the filtering capabilities of the respiratory tract are only crudely estimated by the respirable fraction. Most importantly, for an unvented jet nebulizer used with equal inhalation and exhalation period, half of the inhalable aerosol will be lost to the atmosphere during exhalation, and is not available for inhalation. An in depth discussion of these points is provided by Finlay *et al.* (1997b).

3.4.1.2 Computer Calculations of Regional Dosage

The computer program to calculate the dosages delivered to the three regions of the lungs (extrathoracic, bronchial, and alveolar) is written in FORTRAN and runs on the

IBM RS/6000 family of engineering workstations. This section will describe the necessary input, and outline the calculation procedure.

Three data files are required in addition to the size distribution files from the PDA system. The first file contains the names of the PDA size distribution files. The second data file contains the mass lost during each minute of nebulizer operation, and the concentration of the reservoir solution at the end of the nebulization period. The third data file contains all other required data, as well as the flags for computation options within the code. The reader is referred to Appendix A for a listing of the input files, and a detailed description of the input fields.

Once all data files are read in, the number of droplets exiting the nebulizer in each minute is calculated from the number densities measured by the PDA system and corrected to match the mass lost as a liquid from Equation (3.2). This correction accounts for any droplets not counted due to the optical depth of the cloud. To illustrate how the correction is calculated, consider the *n*th minute of data for the Hudson T Updraft II. The average size distribution measured during the *n*th minute of data collection is integrated to calculate the total mass contained in the droplets. The correction for the *n*th minute is defined as:

$$corr_n = \frac{m_{l,n}}{m_{\text{int},n}} \tag{3.11}$$

where $m_{l,n}$ is the mass lost as liquid in the *n*th minute, and $m_{\text{int},n}$ is the mass obtained by integrating the size distribution for the *n*th minute. The number of droplets in each size class is then multiplied by $corr_n$ to obtain the corrected distribution.

Next, Equation (3.11) is used to calculate the reservoir solution concentration at the end of each minute, or equivalently, the average solution concentration of the droplets during each minute. Multiplying the average solution concentration by the volume of the average particle size for the class gives the average amount of solid in each droplet in the class. This is important since regardless of the hygroscopic growth of the droplet, the amount of solute contained in the droplet is assumed to be constant during its transit through the respiratory tract.

In an unvented jet nebulizer, ambient air is entrained in the mouthpiece to make up the difference between the output flow rate of the nebulizer and the inhalation flow rate of the patient. Here, the aerosol from the nebulizer and the entrained air are assumed to mix instantly, diluting the number density of the aerosol. The heat and water vapour content of the ambient air, and the cooled aerosol from the nebulizer are combined to calculate the temperature and relative humidity of the inhaled air. The droplets are given an initial temperature equal to that of the aerosol exiting the nebulizer.

The next step in the program is the calculation of the droplet growth, and the calculation of the deposition probabilities in each region of the lung model. In each size class, the droplets are assumed to be the same size, and each size class is effectively treated as a monodisperse aerosol. Inclusion of polydispersity in the hygroscopic growth calculations is discussed in Section 2.5.2. Two-way coupled heat and mass transfer is used in the calculations here unless otherwise stated. One-way coupling is available as an option, as is the assumption of inert particles.

The deposition probabilities are calculated using the average size of each particle class in the generation. The deposition model calculates the probability that an inhaled

droplet will deposit in a specific generation. To convert this to a dosage, the total number of inhaled droplets is required.

In an unvented jet nebulizer, the drug inhaled per minute can be determined from the total number density of droplets in each class present in the inhaled air, by the inhalation flow rate, and the total number of seconds per minute occupied by inhalation. For example, it has been suggested that an average breathing cycle consists of a 1.74 second inhalation, 0.2 second inspiratory pause, and a 2.06 second exhalation for a total breathing cycle of 4.0 seconds (ICRP, 1994). In this case, the distribution would be multiplied by 26.1 sec to obtain the number of inhaled droplets in each size class in each minute. Here, for simplicity, we assume equal inspiratory and expiratory times (so the distribution is multiplied by 30.0 sec).

Because of the extremely large number of inhaled droplets in each class, the probability that a droplet will deposit in a generation can be interpreted as the percentage of inhaled droplets depositing in the generation. (The number of inhaled droplets per minute in each particle size class is often $O(10^8)$, while the smallest deposition probabilities are $O(10^{-4})$, so we can expect $O(10^4)$ droplets to deposit in a generation.) Multiplying this percentage by the number of inhaled droplets calculated above gives the number of droplets in each size class that deposit in each generation. Since we know the amount of solids that each droplet contains, the number of droplets deposited in each generation can be easily converted to the mass deposited in each generation, and the dosage of drug delivered to each generation can be determined.

Summing the dose delivered to generations 3 through 19 gives the predicted dosage delivered to the bronchial airways, while the dose delivered to generations 20

through 26 is the predicted alveolar dosage. Total predicted lung dosage is the sum of the bronchial and alveolar dosages. The intersubject variability intervals are converted to dosages in the same way as the mean probabilities.

3.4.1.3 Results

From an initial 2.5 ml nebule of Ventolin®(1 mg/ml salbutamol sulphate), the Hudson T-Updraft II® disposable nebulizer delivered, on average, 0.246±0.017 mg (9.8±0.7% of the nominal dose) of Ventolin® to the extrathoracic region, 0.279±0.11 mg (11.5±.5% of the nominal dose) to the bronchial airways, and 0.173±0.005 mg (4.9±0.3% of the nominal dose) to the alveolar airways. Total lung deposition was 0.402±0.013 mg (16.1±.5% of the nominal dose). The number density of the aerosol was (2.3±0.2) x 10^5 droplets per cm^3, indicating that two-way coupling should be used to correctly account for hygroscopic effects. Dosages are for an average Caucasian male breathing with a tidal volume of 0.75 liters and with an inhalation flow rate of 300 cm^3/s. Ambient conditions for the test were 50% RH, and 23°C.

Region	% of Nominal Dose Delivered	68% Confidence interval
Extrathoracic	9.8±0.7	5.2 - 14.5%
Bronchial	11.2±0.5	7.1 - 15.2%
Alveolar	4.9±0.3	3.4 - 6.4%
Total Lung	16.1±0.5	11.8 - 20.4%

Table 3.5. Regional dosage of Ventolin® delivered to the respiratory tract by the Hudson T Updraft II nebulizer as a percentage of the nominal dose in the nebulizer. Individual dosage for 68% of the population would fall within the given ranges. Calculations are for a tidal volume of 0.75 liters, and an inhalation flow rate of 300 cm^3/s.

3.4.2 Vented Jet Nebulizers

As with the unvented nebulizers, it was first determined that the droplets were in equilibrium with the air exiting the Pari LC+ nebulizer. This was done using the procedure described in Section 3.3 with 12 l/min of dry air supplied to the vent of the nebulizer so that the flow out the mouthpiece equaled the 300 cm^3/s that would be used as the inhalation flow rate in the experiments. It was found that the droplets were in equilibrium at the exit of the nebulizer.

Vented jet nebulizers require a significantly different experimental setup than unvented nebulizers due to the different operating principal. First, both the relative humidity and temperature of the air supplied to the compressor and the vent must be controlled, and be the same. This is done by placing the nebulizer in the same humidity control chamber as the compressor. The mouthpiece of the nebulizer protrudes through the side of the chamber and is connected to a measuring chamber to allow the measurement of the droplet sizes by the PDA system while the inhaled aerosol is being. collected on the filters. The chamber consists of two optically clear lenses oriented perpendicularly to the axes of the transmitting and receiving optics of the PDA system and an airtight volume (see Prokop *et al.* 1995 for a detailed description). It was determined that the measuring volume had no affect on the droplet size measurements by measuring the size of polystyrene spheres of diameters 1.5 μm, 2.5 μm, and 6.0 μm. In each case, the measured size of the spheres was within the 4% error of the PDA system. The measuring volume was connected to a cellulose filter to collect the inhaled aerosol, which was connected to the breathing simulator. See Figure 3.12 for a schematic of the experimental setup

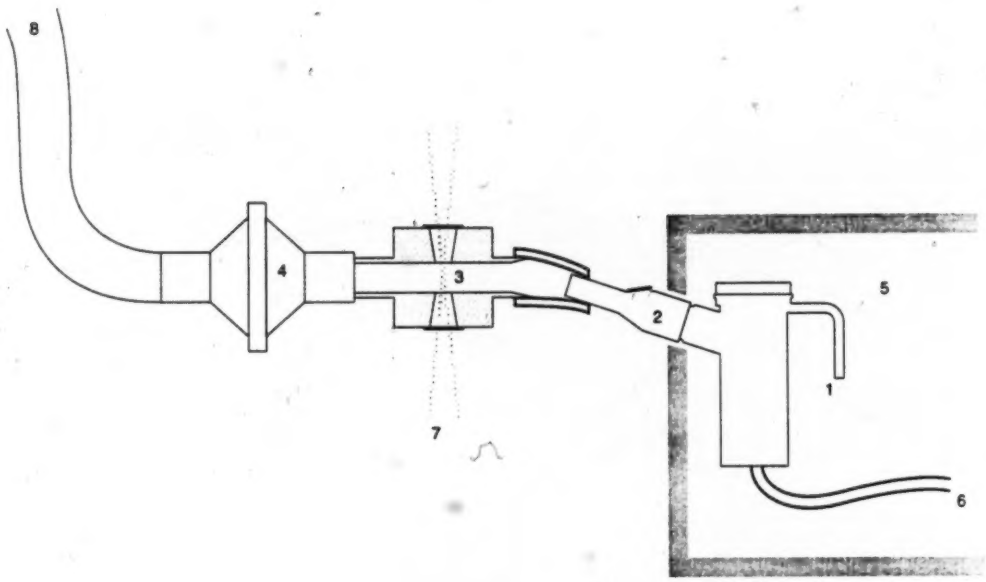

Figure 3.12. A schematic of the experimental setup for a vented jet nebulizer. The nebulizer and mouthpiece (1) and compressor are placed in a chamber (5) with controlled temperature and relative humidity. The nebulizer is attached via hosing to a measuring volume (3) where the size distribution is measured with the PDA (laser beams, 7). The measuring volume is connected via hosing (4) to the breathing simulator

Because aerosol is drawn through the droplet producing region of a vented jet nebulizer, and the output rate of the nebulizer may be dependent on the inhalation flow rate, patient breathing should be simulated to obtain meaningful results. This is done using a computer controlled stepper motor driving a piston connected via hosing to the filter. The in-house motor controller software allows a wide range of breathing patterns, flow rates, and tidal volumes. For these tests, a square wave breathing pattern was used with equal inspiratory and expiratory times and no inhalation or exhalation pause. The tidal volume was set to 0.75 liters, and the inhalation flow rate to 300 cm^3/s.

3.4.2.1 Bench Measurements

Ten Pari LC + nebulizers were tested to give a statistical sample of nebulizer performance. The nebulizers are weighed before and after the addition of the solution to be nebulized. Additionally, the filter and integral holder were weighed before testing. Each nebulizer was then placed in the humidity chamber and connected to the measuring volume. The breathing simulator and the compressor were started simultaneously, and the nebulizer was run until a 15-second pause in output was noted. Size measurements of the inhaled aerosol were taken at one-minute intervals. At the end of the nebulization session, the nebulizer was reweighed, and a sample of the remaining reservoir solution was removed for concentration analysis by freezing point osmometry. The filter was then weighed, and the amount of solids collected determined by the procedure described in Section 3.3.3.

An additional concern in this methodology is the connection volume between the mouthpiece and the filter. If this volume is a significant percentage of the tidal volume, then the mass of droplets collected on the filter will not be an accurate measurement of the droplets actually inhaled. To correct for this, the masses collected on the filter are multiplied by a scaling factor defined as:

$$scale = \frac{V_T}{V_T - V_{cv}} \tag{3.13}$$

where V_T is the tidal volume, and V_{cv} is the connection volume. The connection volume was measured to be 102 cm^3, so the scaling factor is 1.157 for the 0.75 liter tidal volume used here.

After correction for the connection volume, the average mass collected on the filters was 0.386±0.012 g, and the average mass of solids collected on the filter was 5.55±0.18 mg. The average MMD of the aerosol was 5.91±0.09 μm, and the GSD was measured at 1.72±0.01. The average mass lost during the nebulization session was 1.27±0.04 g, and the average concentration of the reservoir solution was 1.21±0.02 mg/ml. A respirable fraction of 52% can be calculated from the size distribution as for unvented nebulizers. However, because the mass collected on the filters is only inhaled mass, a nebulizer efficiency and delivered respirable fraction cannot be compared directly with those calculated for the Hudson T-Updraft II.

3.4.2.2 Calculation of Regional Dosages

After reading in the data files, the aerosol size distributions measured at one minute intervals during the nebulization session are averaged to obtain an average distribution for the entire session (It was found that the MMD and GSD of the aerosol changes very little during the nebulization session). The averaged distribution is then integrated and scaled as described in Section 3.4.1.3 with the total inhaled mass collected on the filter to calculate the total number of droplets inhaled during the nebulization session. The total mass of inhaled solids is then distributed though the droplets so that each droplet has the same concentration (this is justified by knowing that the droplets are in equilibrium when they exit the nebulizer, therefore they all have the same solution concentration). After this, the procedure to calculate the regional dosages is the same as for unvented jet nebulizers.

3.4.2.3 Results

On average, the Pari LC+ nebulizer delivered an estimated 0.498±0.008 mg (19.9±0.3% of the nominal dose) of Ventolin® to the respiratory tract from an initial 2.5 ml nebule (1 mg/ml salbutamol sulphate). The estimated dose was distributed as follows: 0.172±0.005 mg (6.9±0.2%) to the extrathoracic region, 0.236±0.006 (9.4±0.2%) to the bronchial region, and 0.090±0.003 (3.6±0.1%) to the alveolar region. These estimated dosages and the estimated intersubject variability ranges are given in Table 3.6. The number density of the aerosol was (8.8±0.3) x 10^5 droplets/cm^3. Deposition is for an average Caucasian male breathing with a tidal volume of 0.75 liters and with an inhalation flow rate of 300 cm^3/s. Figure 3.13 compares the output of the Pari LC+ and the Hudson T Updraft II.

Region	% of Nominal Dose Delivered	68% Confidence interval
Extrathoracic	6.89±0.2	4.0 - 9.81%
Bronchial	9.44±0.2	5.88 - 13.0%
Alveolar	3.59±0.1	2.35 - 4.83%
Total Lung	13.03±0.3	9.26 - 16.8%

Table 3.6. Predicted regional dosage of Ventolin® delivered to the respiratory tract by the Pari LC+ nebulizer as a percentage of the nominal dose in the nebulizer. The 68% confidence interval indicates the range within which estimated dosages for 68% of the population would fall. Calculations are for a tidal volume of 0.75 liters, and an inhalation flow rate of 300 cm^3/s.

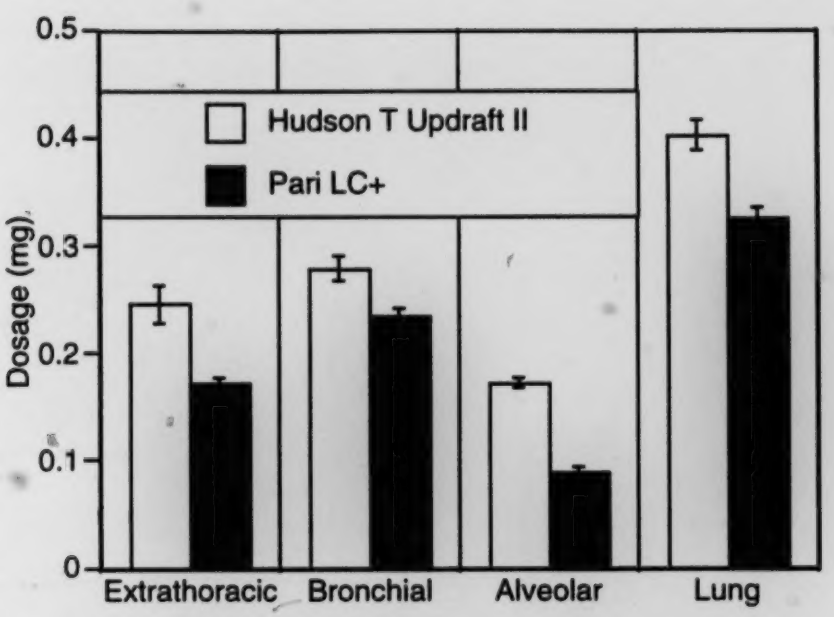

Figure 3.13. The regional dose delivered by the Hudson T Updraft II and the Pari LC+ nebulizers. Test conditions were 50% RH, 23°C. Dosages are for an average Caucasian male with an inhalation flow rate of 300 cm^3/s and a tidal volume of 0.75 liters. Error bars on the graph indicate the standard error in the measurements.

3.4.3 The Effect of Tapping

Tapping the side of the nebulizer during operation promotes the return of nebulizer solution attached to the sides of the nebulizer by surface tension (in the form of drops), to the reservoir for renebulization. This is particularly important during the final phase of the nebulization session when the nebulizer is sputtering. Stapleton *et al.* (1994) predicted the regional dosage delivered by the PulmoNeb® disposable nebulizer with the above procedure with two protocols: first with no tapping, and the second where the nebulizers were tapped with a finger on the side of the nebulizer at a rate of approximately 4 taps per second whenever the nebulizer was not outputting aerosol.

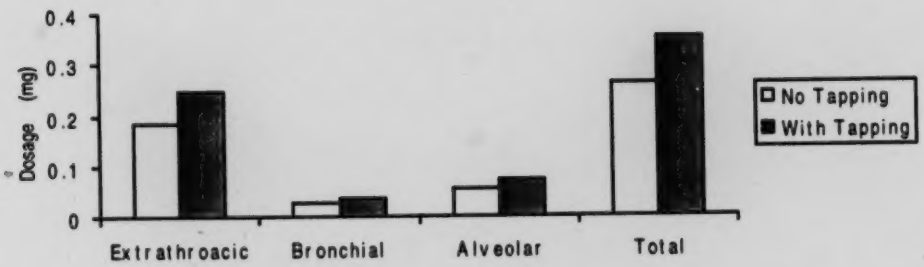

Figure 3.14. The effect of tapping the nebulizer at a rate of approximately 4 taps per second during the nebulization session. The total dosage delivered to the respiratory tract increased from 0.261±0.005 mg (10.4±0.2% of nominal dose) to 0.352± 0.006 mg (14.1±0.2% of nominal dose), an increase of 35%. The regional distribution of the dose did not change. The inhalation flow rate was 300 cm^3/s tidal volume 0.75 liters, and ambient conditions were 23°C and 26% RH. All values mean ± standard error.

They found that the nebulization session increased from 4 to 6 minutes, and that the mass output by the nebulizers increased by 35%.

When the tapping protocol was used, the estimated dose of Ventolin® delivered to the respiratory tract increased from 0.261±0.2 mg (10.4% of the nominal dose) to 0.352±0.006 mg (14.1% of the nominal dose), an increase of 35% over the estimated dosage delivered when no tapping was used. Note, however, that the relative regional distribution of the estimated dosage is not changed.

3.4.4 Effect of different treatments of hygroscopic growth

The hygroscopic growth calculations can be performed assuming either two-way or one-way coupling between the droplets and the surrounding air, or by assuming that the droplets do not change size. Finlay & Stapleton (1995) showed that for polydisperse aerosols typical of those produced by nebulizers, differences in the calculated dosages for the three calculation modes can be as high as 137%. In the tests discussed above, the

Hudson T Updraft II produced an aerosol with approximately $2.3x10^5$ inhaled droplets/cm^3, and the Pari LC+ produced an aerosol with approximately $8.8x10^5$ inhaled droplets/cm^3. Both of these are in the range in which Finlay & Stapleton suggest two-way coupling should be used. However, because of the added expense of two-way calculations, it is useful to consider how the different hygroscopic treatments might affect the regional dosages for the nebulizers here.

As can be seen in Table 3.7, using one-way coupling to calculate the hygroscopic growth of the droplets results in a decrease in the predicted extrathoracic deposition and an increase in the predicted alveolar deposition. For the Hudson T-Updraft II, the difference in the predicted extrathoracic deposition between two-way and one-way coupling is approximately 40%, and for the Pari LC+ it is approximately 30%. The differences between the predicted alveolar dosages 53% and 47% respectively, and the differences between the predicted bronchial dosages are approximately 13% and 6% respectively. For the two nebulizers considered here, one-way coupling in the hygroscopic growth calculations will lead to significant errors in the estimated regional dosages.

In the case of the Pair LC+, assuming inert particles is superior to 1-way coupling, resulting in differences of less than 5% for all estimated dosages between two-way coupling and inert particles. For the Hudson T-Updraft II, the difference in the estimated dosage between two-way coupling and inert particles is as high as 15%, still significantly less than the difference between one-way and two-way coupling. The cause of this effect is that the high number densities of the aerosol are likely buffering the hygroscopic

Nebulizer	Region	2-way coupling	1-way coupling	Inert particles
Hudson T Updraft	Extrathoracic	9.8±0.7	7.0±0.6	10.6±0.7
II	Bronchial	11.2±0.5	9.9±0.4	11.4±0.4
	Alveolar	4.9±0.2	7.5±0.4	4.2±0.2
	Total Lung	16.1±0.5	17.4±0.5	15.7±0.4
Pari LC+	Extrathoracic	6.8±0.2	5.2±0.4	6.6±0.3
	Bronchial	9.4±0.2	8.9±0.3	9.3±0.2
	Alveolar	3.6±0.1	5.3±0.3	3.8±0.2
	Total Lung	13.0±.03	14.2±0.4	13.1±0.3

Table 3.7. The percent of the nominal dose put in the nebulizer delivered to different regions of the respiratory tract calculated with three different treatments of the hygroscopic growth calculations. Predicted total lung deposition is the sum of alveolar and bronchial deposition. All values are mean ± standard error.

growth of the droplets. It is important to note that this may not be the case with all nebulizers.

Recently, Finlay *et al.* (1997c) studied the effect of the different treatments of the hygroscopic effects on the deposition of aerosol from 7 different nebulizers. They found that at ambient humidities of approximately 90%, two-way coupling, one-way coupling, and neglecting hygroscopic growth entirely all gave similar results. At lower ambient humidities, they found errors up to 65% occurred by using a one-way coupled model. These results are consistent with those found here.

3.5 Comparison with other methodologies

To the author's knowledge, there are no other published models for predicting the regional dosage of nebulized drug delivered to the respiratory tract. Other models for

calculating the regional deposition probabilities of inhaled particles were discussed throughout Section 2. Methods for characterizing the performance of nebulizers were briefly discussed above, and by Finlay *et al.* (1997b).

As was discussed briefly in Section 3.3.2.1, Ferron *et al.* (1997) investigated the stability of aqueous droplets produced by jet nebulizers using a hygroscopic growth model similar in some ways to that presented here. While the benchtop data collected from the nebulizers is also similar, hygroscopic growth model is quite different from that presented here. It is useful to compare the two methodologies in some detail.

Briefly, Ferron *et al.* measure m_{out}, the total mass output of the nebulizer, and m_s, the total mass of solids leaving the nebulizer by weighing the nebulizer, and measuring the solids output over the nebulization session (e.g. by collecting the dried solids on a filter). Next, the mass of liquid in the droplets immediately after creation is calculated by dividing m_s by the initial concentration of the nebulizer reservoir solution. Any additional mass lost from the nebulizer is assumed to have evaporated from droplets that impact on the walls of the nebulizer that have returned to the reservoir. The water vapour which evaporates from droplets returning to the nebulizer is assumed to instantly mix with the air at the venturi and this provides the initial water vapour content of the air for the calculations. The size distribution of the droplets immediately after creation is assumed to be either a distribution measured at the exit of the nebulizer, or is calculated by drying the droplets, measuring the distribution of the dry particles, and inferring an initial size based on a growth factor (the dry residual method, see e.g. Sterk *et al.* 1984). The temperature of the air and the droplets are assumed to be constant and equal to ambient conditions. (This assumption is in error, as will be discussed shortly). From

these initial conditions, the growth of the droplets is calculated using a methodology similar to the one-way coupled model described here, with the difference that after each time step, any mass gained/lost by the droplets is subtracted/added to the water vapour content of the surrounding air.

Ferron *et al.* present calculations for the DeVilbiss PulmoNeb® tested here, and indicate that the aerosol is relatively stable after only 0.1 second, less than the average residence time of 0.5 seconds for a droplet in the nebulizer, and supporting the conclusion presented here that the droplets are in equilibrium when exiting the nebulizer. However, Ferron *et al.* suggest that this is not be the case for other nebulizers, which differs from the suggestion of the results presented here, and from experience with other nebulizers in our laboratory. Possible sources for the discrepancy can be seen by comparing the details of each method.

The differences between the methods are subtle, yet important. First, in the methodology presented here, the growth calculations are begun after the droplets exit the nebulizer, while Ferron *et al.* begin the calculations immediately after droplet creation. While the size distribution of the droplets can be easily measured at the exit of the nebulizer and their concentration calculated by the procedure detailed in Section 3.3, the distribution at the creation point must be assumed or indirectly calculated. This adds another source of uncertainty to the accuracy of the size distribution beyond those associated with the measurement method, and neglects any change in the solute content of the droplets. (It is well known that the concentration of the reservoir solution increases with time, and often this increase is as high as 50% above the initial concentration. Using a constant growth factor, this could have two effects: first, the size distribution of the

droplets produced at the end of the nebulization session will be overestimated, and second, if the solute particles are collected over an entire nebulization session, the GSD of the distribution may be overestimated.)

Secondly, and more importantly, Ferron *et al.* neglect the cooling of the reservoir solution and the output air. At the end of one minute of operation, the temperature of the air exiting the PulmoNeb nebulizer is 3 °C below ambient, so the initial water vapour concentration calculated by Ferron *et al.* corresponds to 95% relative humidity, compared to the 80% calculated using ambient temperature. After two minutes of operation, the temperature of the air exiting the nebulizer has dropped another degree, and the calculated relative humidity is now over 100%, which according to the method of Ferron *et al.* indicates that the droplets should no longer shrink, and therefore the concentration of the solution in the nebulizer should no longer increase. This is not the case, as can be seen in Table 3.1, where the concentration continues to increase for 7 minutes. The temperature profiles for the other nebulizers used by Ferron *et al.* are not known, although it is common for the output air to drop 5 to 10 degrees C in less than 2 minutes (Phipps & Gonda, 1990). In general, the initial conditions used by Ferron *et al.* are only representative of the first few seconds of nebulizer operation, but are not representative of an entire nebulization session.

The third difference is in the treatment of the coupling between the droplets and the surrounding phase. For one-way coupled calculations, the equations used by both methods are similar and only differ in their treatment of the vapour pressure reduction at the droplet surface due to dissolved solids (Ferron *et al.* assume dilute solutions and use Raoult's Law; here, a nonlinear equation for NaCl is used), and the treatment of some

	Ferron et al. (1997)	This Model	Ferron et al. (1997)	This Model
Time	0.1 sec	0.1 sec	3.0 sec	3.0 sec
Salt MMD	2.2 μm	2.68 μm	2.15 μm	2.65 μm
Salt GSD	2.87	2.56	2.44	2.55
Mass MMD	3.6 μm	3.03 μm	2.45 μm	3.00 μm
Mass GSD	2.3	2.27	2.53	2.26
Final Temperature	20°C	16 °C	20°C	16°C
Relative Humidity	87%	99.5%	99.1%	99.5%
Water vap. conc.	15 μl/ml	13 μl/ml	17 μl/ml	13 μl/ml

Table 3.8. Comparison of the results of Ferron *et al* (1997) Figures 6 & 7 to the model presented here for an aerosol with an MMD of 2.8 μm and a GSD of 2.3. Results from our model for the droplet growth 30 seconds after creation differ in the 5th significant digit from those at 3.0 seconds and are not presented.

parameters such as the diffusion coefficients (Ferron *et al.* assume constant values, while values which change with temperature are used here). These differences have been found to have minor effects on the growth rates (Stapleton *et al.* 1995).

However, for two-way coupled calculations, the treatment differs dramatically. Ferron *et al.* assumes quasi-steady droplet growth, and calculate the mass added to the surrounding phase from the evaporation of the droplets. A similar process could be applied to the temperature of the surrounding phase, although in this specific instance, Ferron *et al.* assume that the temperature of the droplets and the surrounding air is constant and equal to the ambient temperature. The treatment of the coupling of the heat and mass transport between the continuous phase and the droplets is inconsistent since it assumes that mass transfer can occur between the droplets and the continuous phase

without heat transfer. Using this explicit scheme, the mass flow from each particle size class remains uncoupled from the others and can be calculated individually. In the model presented here, the droplet growth equations for all particle size classes remain coupled, and an implicit method is used to solve for all the droplet growth rates, droplet temperature, and the temperature and humidity of the surrounding phase simultaneously.

It is useful to compare the two models using the same initial conditions. To do so, the data from the Pari IS-2 nebulizer given by Ferron *et al.* will be used since it shows the greatest variation in the aerosol properties. The initial conditions for the run are an aqueous aerosol of 0.9% NaCl by weight with an MMD of 2.8 μm and a GSD of 2.3. The initial temperature of the air and droplets is 20.0°C, and the initial RH is 67%. By integrating the lognormal distribution, 2.3×10^7 droplets/cm^3 are required to obtain the initial concentration of water of 11.892 μg/cm^3 calculated by Ferron *et al.*

The droplet growth was calculated at the following times after droplet creation: 0.1 seconds, corresponding approximately to the average residence time of the droplets in the nebulizer; 3.0 seconds, corresponding to the time Ferron *et al.* suggest that is required for the droplets to achieve equilibrium; and 30.0 seconds, as a check to ensure that the droplets are in equilibrium.

As can be seen in Table 3.8, Ferron *et al.* (1997) predict significant changes in both the MMD and GSD of the aerosol, while the model presented here indicates far smaller changes in these quantities. Most importantly, the hygroscopic growth model presented here does not predict significant changes in the properties of the aerosol after 0.1 seconds, indicating that the droplets are in equilibrium at that time. Changes in the MMD and GSD of the salt distribution with respect to the mass distribution seen with the

present model are consistent with a 0.9% increase in the average concentration of the droplets compared to the initial concentration.

4. CFD studies of particle deposition in the extrathoracic region of the respiratory tract

4.1 Introduction

The modeling of aerosol deposition in the human respiratory tract described in the previous sections of this thesis provides a powerful tool for the evaluation of inhaled aerosols and the devices which produce them. However, at best they provide estimates of the dosage delivered to three regions of the respiratory tract: the extrathoracic region, the tracheo-bronchial region, and the alveolar region; but they do not predict local sites of deposition within the regions, or local deposition patterns within specific airways. Experimental investigation can provide some insight into these areas, but such investigations depend on the availability of accurate casts (and therefore must deal with issues such as post-mortem chages in the airway geometry). Additionally, *in situ* experiments are difficult owing to the size and accessibility of the airways, often forcing the experimentalist to use surrogate geometries (usually based on a Weibel lung model).

Computational fluid dynamics, or CFD, is a popular research and design tool in many engineering disciplines and complements experimental research by providing the ability to manipulate specific features of the flow (e.g. the inlet profile) and by providing a

different paradigm from which to view a fluid flow problem. CFD refers to the use of numerical methods to solve the Navier-Stokes equations, which are the partial differential equations governing the flow of a single-phase Newtonian fluid. CFD can produce detailed simulations of fluid flow, and particles can be tracked through the flow to predict local deposition sites, and filtering efficiencies. The benefits of using CFD to study air flow and particle deposition in the respiratory tract include the use of more realistic geometric lung models, and not requiring drastic assumptions about the flow regime (i.e. 1-D plug flow).

Recently, commercially distributed, general purpose CFD software packages are becoming popular research tools in many areas, including aerosol research. Contributing to this increasing popularity are easy-to-use graphical interfaces, inexpensive computers, and robust solvers. However, CFD programs have not matured enough that they can be used without considerable attention to the validity of results they produce. This is true for codes written for specific geometries, and even more so for commercial, general purpose software packages. It is far beyond the scope of this thesis to discuss all of the issues involved in using CFD, but there are numerous textbooks which discuss in detail the use of CFD techniques for obtaining flow simulations, from an introductory level (e.g. Anderson, 1995) through to an advanced level (e.g. Fletcher, 1991) that a reader can reference. Additionally, Finlay *et al.* (1996) briefly discuss some of the issues involved in the use of these techniques in the context of simulating fluid flow and particle deposition in the respiratory tract. Some of the issues discussed in these references are reviewed here for completeness.

One of the main issues in the use of CFD is the nature of the equations being solved. The Navier-Stokes equations are a system of three-dimensional, nonlinear, coupled partial differential equations, and the complete equations (without simplifying

assumptions) contain all of the physics governing the motion of Newtonian fluids. Unfortunately, the highly nonlinear, three-dimensional nature of the equations means that analytical solutions cannot be obtained except in a handful of simple geometries (see e.g. Wang 1991, Panton, 1996). Furthermore, the complete Navier-Stokes equations are impractical to solve numerically in all but the simplest of geometries, and on the computers of today, solution in many geometries is only possible if certain aspects of the flow, such as turbulence, are modeled.

Additionally, the nature of the Navier-Stokes equations themselves make it difficult to extrapolate from one geometry to another, so that even experienced CFD users may be able to supply little *a priori* knowledge regarding the flow in a new geometry.

The purpose of this section of the thesis is to investigate the usefulness of CFD techniques for studying fluid flow and aerosol deposition in the respiratory tract. A commercial general purpose CFD software package (TASCflow3D, Advanced Scientific Computing Ltd., Waterloo, ON) is used to study the fluid flow and particle deposition in a novel geometrical model of the extrathoracic airways of the respiratory tract (c.f. section 3.3 for a complete description). TASCflow3D solves the Reynolds-averaged Navier-Stokes equations on block-structured, non-orthogonal, body fitted grids with equal-order velocity-pressure interpolation (Prakash & Patankar, 1985). TASCflow3D is unique among commercial CFD codes in that the equations are written in strong conservation form and solved using a finite volume method, while a finite element method is used to describe the geometry and grid transformations. (The strong conservation form of the Navier-Stokes equations provides some programming convenience, as well as some numerical advantages over a non-conservation formulation. Finite volume methods provide an advantage in that continuity is satisfied at each iteration, not only when the solution has converged. See Anderson (1995) for a detailed explaination.)

The CFD software will be tested in three stages. First, the particle deposition will be calculated for flow through round tubes with a 90° bend and compared to experimental results available in the archival literature. Second, the flow and particle deposition in a geometry similar to the model throat used with an impinger (USP, 1995) was calculated. The deposition patterns and filtering efficiencies were determined experimentally by viewing the deposition of a radiolabelled aerosol in a fiberglass model of the geometry, then comparing with the CFD results. Finally, the flow and particle deposition in a novel throat geometry was calculated and compared with experimentally determined filtering efficiencies and deposition patterns from viewing the deposition of radiolabelled aerosol in a fiberglass model of the geometry. Additionally, the filtering efficiencies of the model throat are compared with estimates of the *in vivo* deposition probabilities in the extrathoracic region available in the archival literature.

A priori, CFD is expected to perform poorly in the USP model throat and the physiologically realistic throat model. First, the Reynolds numbers of the flows in these models is on the order of a few thousand, so transition flow between laminar and turbulent flow can be expected. (In the case of the USP model throat, a scale model of the geometry was tested in a water channel with fluorescent dye illuminated by a sheet laser, and turbulent flow was observed. In the extrathoracic airways, the flow is known to be turbulent, see e.g. Dekker, 1961) Current turbulence models are known to perform poorly with these flows. Additionally, turbulence models are known to perform poorly in flows such as these with recirculation regions and curved streamlines.

Relatively few articles are available in the archival literature describing the use of CFD for studying the fluid flow and particle deposition in the respiratory tract. CFD has been used successfully to study the air flow and particle deposition in airway bifurcation's corresponding to the 4th to 5th bifurcation in a Weibel lung (see e.g. Hofmann &

Balàshàzy 1991, Balàshàzy & Hofmann 1993, Hofmann *et al.* 1996) where the Reynolds number is on the order of a few hundred, and the flow can be expected to be laminar. Martonen *et al.* (1993) used a commercial CFD package to solve the two-dimensional, laminar, Navier-Stokes equations in an axisymmetric model of the larynx, trachea, and main bronchi. Unfortunately, the presented solution is for laminar flow, when the flow in the trachea is clearly turbulent at the flow rates studied (see Section 1.3 for a detailed discussion and references), so the results have limited applicability to the flow in a human.

Recently, Yu *et al.* (1996) used a commercial CFD code to study the flow patterns and the deposition of ultrafine particles in a model of the trachea and main bronchi and show reasonable agreement with the experimental data of Schroter & Sudlow (1969), who experimentally studied the flow patterns in airway bifurcation's over a wide range of Reynolds numbers. While the computational results seem to be sufficient for the bifurcation model studied, caution must be used when applying these results to the respiratory tract because, similarly to the above mentioned work, laminar flow is assumed in the trachea. Additionally, Yu *et al.* comment on the sensitivity of their results to the inlet boundary conditions, and yet they neglect any effects that the larynx may have on the flow in the trachea.

Katz & Martonen (1996a) present numerical simulations of flow through a model of the larynx using FIDAP (Fluid Dynamics International, Inc., Evanston IL), a commercially available CFD package that uses a finite element method to solve the Navier-Stokes equation. The geometry is based on laryngeal casts (Martonen & Lowe, 1983), with the glottal opening approximated as an ellipse. The oral and pharyngeal cavities are not simulated, and the trachea is assumed to be a circular cylinder. Three glottal openings are studied, corresponding to sedentary, light work, and heavy work flow rates (15, 30, and 60 liters/min., respectively). In the companion paper, Katz & Martonen (1997b) use the

particle tracking features of FIDAP to predict time averaged particle paths through the geometry. However, the purpose of the article is to investigate the air flow through the larynx using the tracks of massless particles to visualize the flow field. No information on the size of the particles is given, and the filtering properties of the model are not investigated.

4.2 Calculation of particle trajectories

In CFD, particle deposition probabilities are calculated by tracking individual particles through the geometry, and if a particle contacts a wall, then the particle is said to have deposited in the geometry, and the deposition location is recorded. By tracking many particles through the geometry, a statistical description of particle deposition can be obtained.

Particle trajectories are calculated by solving the equation of motion of a rigid sphere in the flow which was derived by Basset, Boussinesq and Oseen (Hinze, 1975), and is discussed in detail by Maxey & Riley (1983) and Berlemont *et al.* (1990), and is briefly reviewed here. In this work, we assume one-way coupling between the particles and the flow, that is, the flow influences the paths of the particles, but the particles do not affect the flow. This is a reasonable assumption for the particle number densities output by jet nebulizers. (It is important to distinguish the coupling used with the particle tracking and the coupling used with the hygroscopic growth calculations. Two-way coupling between the droplets must be considered with the hygroscopic growth calculations. The source terms in the momentum equations from the particles are approximately 5 orders of magnitude lower than the other terms of the momentum equations for the aerosol number densities typically output by jet nebulizers, and may be ignored). In this preliminary work,

we choose to avoid the added complications of hygroscopic particles, and only consider inert particles.

The equation of motion for a particle traveling in a continuous fluid is (Maxey & Riley, 1983):

$$m_p \frac{dv_p}{dt} = 3\pi\mu d C_{cor}\left(v_f - v_p\right) + \frac{\pi d^3 \rho_f}{6}\frac{dv_f}{dt} + \frac{\pi d^3 \rho_f}{12}\left(\frac{dv_f}{dt} - \frac{dv_p}{dt}\right) +$$

$$+ \frac{3}{2} d^2 \sqrt{\pi \rho_f \mu} \int_{t_0}^{t} \frac{\left(\frac{dv_f}{dt'} - \frac{dv_p}{dt'}\right)}{\sqrt{t - t'}} dt' + F \qquad (4.1)$$

where m_p = particle mass
v = instantaneous velocity
ρ = density
μ = dynamic viscosity
F = external forces on the particle (e.g. gravity, electrostatic forces);
C_{cor} = drag coefficient for spheres (dependant on Reynolds number)

and t_0 is the starting time The subscript, f, refers to the fluid and the subscript, p, refers to the particle. The first term on the right-hand side of Equation (4.1) is the Stokes drag (or viscous drag) on the particle. The second term is the force applied on the particle from the stress gradients (usually pressure) in the fluid surrounding the particle. The third term on the right-hand side is the virtual mass term, and accounts for the force necessary to accelerate the virtual mass of the fluid in the volume occupied by the particle. The fourth term on the right-hand side is the Bassett history term, and is essentially an unsteady correction to the Stokes drag term.

For particles that are significantly heavier than the surrounding fluid, Equation 4.1 reduces to:

$$\frac{\pi d^3 \rho_p}{6}\frac{dv_p}{dt} = 3\pi\mu d C_{cor}\left(v_f - v_p\right) + F \qquad (4.2)$$

Here, the force on the particle is essentially given by the sum of the Stokes drag and any external forces.

To account for the influence of turbulent fluid fluctuations on particle motion, an eddy lifetime model is used. It is assumed that a single characteristic eddy can be defined for the flow with a characteristic fluctuating velocity, v_f', lifetime, τ_e, and length, l_e, which are calculated from the local turbulence properties of the flow. When a particle enters an eddy, the fluctuating velocity v_f' is added to the mean fluid velocity to obtain the instantaneous fluid velocity used in Equation. (4.1). The particle will remain in the eddy, responding to the same instantaneous fluid velocity as long as the particle/eddy interaction time is less than the eddy lifetime, τ_e, or the displacement of the particle relative to the eddy is less than the eddy length, l_e. If either of these conditions is exceeded, the particle is assumed to be entering a new eddy with new characteristic v_f', τ_e, and l_e.

The fluctuating velocity, eddy lifetime and length are calculated based on the local turbulence properties of the flow:

$$v_f' = \Gamma\left(\frac{2k}{3}\right)^{1/2} \tag{4.3}$$

$$l_e = \frac{C_\mu^{3/4} k^{3/2}}{\varepsilon} \tag{4.4}$$

$$\tau_e = \frac{l_e}{(2k/3)^{1/2}} \tag{4.5}$$

where k and ε are the local turbulence kinetic energy and dissipation, C_μ is a turbulence constant, and Γ is a normally distributed random number to account for the randomness of turbulence around a mean value. Note that each eddy will have three fluctuating velocities (u', v', w'), one for each coordinate direction, and that each is calculated separately using Equation (4.3).

Particles are distributed randomly over the inlet boundary, and are tracked individually through the computational domain using an explicit Euler integration of the particle velocity over the timestep δt,

$$x_i^n = x_i^o + \frac{dx_i^o}{dt}\delta t \tag{4.6}$$

where the superscripts o and n refer to the old and new values, respectively, and the particle velocity is $v_{p_i} = dx_i/dt$. For heavy particles as considered here, the velocity at each timestep is calculated using the analytical solution to Equation (4.2) given by:

$$v_p = v_f + \left(v_p^o - v_f\right)\exp\left(\frac{-\delta t}{\tau}\right) + \tau F \exp\left(\frac{\delta t}{\tau}\right) \tag{4.7}$$

where

$$\tau = \frac{d^2}{18\mu C_{cor}}\left(\rho_p + \frac{\rho_f}{2}\right) + \frac{d}{C_{cor}}\sqrt{\frac{\rho_f \delta t}{4\pi\mu}} \tag{4.8}$$

Here, v_p^0 is the particle velocity at the start of the time step.

The timestep δt used in the calculation of the particle trajectories is independent of the timestep used in the main flow calculations, and is limited by three criterion:

1. a particle cannot travel beyond a flux element boundary;
2. a particle can travel a maximum of 1/5 of the characteristic flux element length (this fraction is user definable, and the default value of 1/5 is used here);
3. for turbulent flows, a particle cannot travel beyond an eddy, and the timestep must be smaller than the eddy lifetime.

The particles are tracked until they either contact a wall of the geometry, or until they exit the geometry through the outlet boundary.

4.3 Turbulence models and boundary conditions for turbulent flows

Before modeling a flow using current CFD methods, it must be decided whether the turbulent or laminar model equations are to be used. The USP model throat and the physiologically realistic throat model described in the next section will be studied at a flow rate of 28.3 liters/min, corresponding to the flow rate through an Andersen Mark II cascade impactor. The Reynolds number of the flow at the exit of the impinger model throat is approximately 1550, slightly less than the transition value of 2300 for straight tubes. However, because of the complex geometry, turbulence may be present in the flows. A scale model of the geometry was built and tested in a water channel, and turbulent flow was observed. In the physiologically realistic model described in Section 4.4, the Reynolds number through the larynx at the same flow rate is 2600, so turbulence may be expected. Recall from Section 2.3 that turbulence is present in tracheal flow at Reynolds numbers lower than those considered here. Thus for both geometries, the flow is unlikely to be laminar. The choice of turbulence model used in the calculations is an important consideration as it has implications on the structure of the grid that can be used. (Two turbulence models are available in TASCflow3D, a standard $k-\varepsilon$ model, and a two-layer model which will be described later in this section) The reader is referred to one of the many texts on turbulence modeling (e.g. Wilcox, 1993) for a complete discussion of this topic, and only a few of the issues directly applicable to the work here will be discussed.

It can be shown that the equations used in a standard $k-\varepsilon$ turbulence model do not accurately predict the flow profiles near solid boundaries (see e.g. Wilcox 1993). Therefore, unsatisfactory results may be obtained if an attempt is made to apply the no-slip boundary condition for fluid flow at a wall and integrate through the boundary layer. To

avoid this, an algebraic expression is used to calculate values of the turbulence kinetic energy and the dissipation at the grid point closest to the wall. These algebraic expressions are called wall functions, and are only valid in the log layer, normally considered to be $30 \leq y^+ \leq 500$, where y^+ are dimensionless wall units defined as:

$$y^+ = \frac{u_\tau y}{\nu} \tag{4.9}$$

where: $u_\tau = \sqrt{\tau_w / \rho}$ is the friction velocity
τ_w = wall shear stress
y = distance above the wall
ν = fluid kinematic viscosity

Therefore, to use wall functions, the first grid point away from the wall should be at a y^+ value of $30 \leq y^+ \leq 500$, and grid generation often becomes an interactive process where a grid is created, then a solution obtained, and it is then determined if the grid point closest to the wall requires repositioning.

In the case of the USP model throat, this creates a difficulty as the diameter of the inlet tube is on the order of a few hundred y^+ units in diameter. This would require that the first grid point be approximately 1/4 of the way from the wall to the centerline, and more than 3/4 of the cross sectional area of the flow would be predicted by the first layer of nodes away from the wall.

Overcoming these shortcomings requires the use of a low Reynolds number turbulence model. Often, damping functions are added to the standard $k-\varepsilon$ model equations in the region $y^+ \leq 50$ to allow integration through the viscous sublayer. TASCflow3D uses a different approach, and uses a one-equation turbulence model near the wall, and a standard $k-\varepsilon$ turbulence model away from the wall. (The model used here solves the turbulence kinetic energy equation and uses an algebraic expression with a damping function to calculate the dissipation. The equation for the turbulent viscosity also

contains a damping function.) Patel *et al.* (1985) compares this method with other low Reynolds number turbulence models and finds that it is both robust and accurate. If a low Reynolds number turbulence model is used, then the grid points near the wall must properly resolve the viscous sublayer, which typically requires on the order of 10 nodes below $y^+ \approx 10$.

4.4 Physiologically realistic throat model

Qualitative descriptions of the extrathoracic region of the airway are available in anatomy textbooks (c.f. get some anatomy text reference). These textbooks provide the reader with a detailed description of the features of the airway, their function, and their location in relation to other structures. However, they do not provide the quantitative information necessary to construct a model for use with CFD.

Taking measurements of the extrathoracic airways is complicated by the presence of soft tissues, for example, the tongue. It is well known that the tongue changes the shape of the pharynx and mouth for the production of speech (c.f. Baer *et al.*, 1991, Sorokin, 1992), and the glottal width varies through the breathing cycle (Brancatisano *et al.* 1983). The presence of these soft tissues also complicates the use of casts, as it is difficult to preserve the shape of these tissues post mortem.

Here, we choose to base our geometrical model on data from computed tomography (CT) scans, magnetic resonance imaging (MRI) scans, and direct observation of living subjects. Where possible, the model is based on information available in the archival literature, and supplemented with measurements from CT scans of patients (n = 10) at the University of Alberta Hospital with no visible airway abnormalities, and by personal observation of living subjects. By using these dimensions, and simple geometric shapes, a model of the extrathoracic airways suitable for study with CFD is developed.

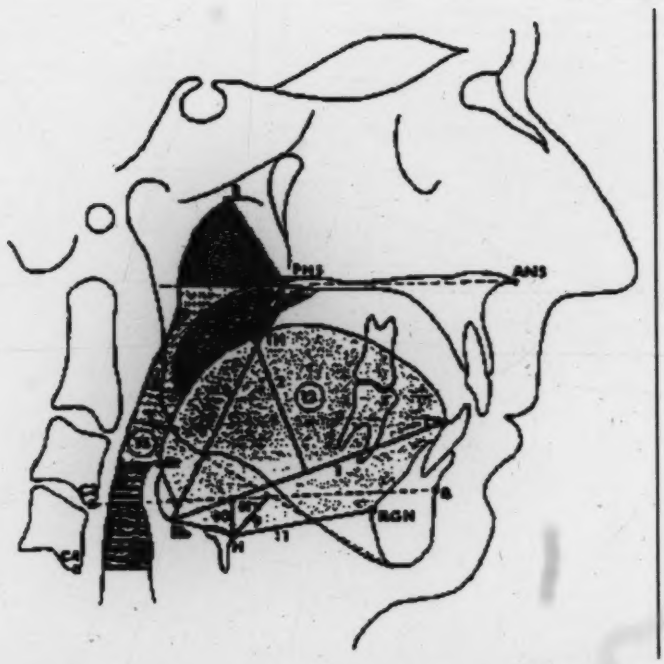

Figure 4.1. A schematic representation of the mouth and pharynx showing the cephalometric variables measured by Pae *et al.* (1994). Dimensions used in the creation of the model throat described here include: 1, tongue length; 2, tongue height; 4, maximum palate thickness; 7, inferior airway space; 8, vertical airway length.

Description of the model will proceed from the trachea to the mouth. A basic knowledge of the anatomy of the extrathoracic airways is assumed, and the reader is referred to an anatomy text for a description of the anatomical terms.

The trachea is a nearly cylindrical tube contained by a series of cartilaginous rings. It's length and diameter are well studied, and we adopt the values specified in the Weibel 'A' model scaled to 3 liters (see Table 2.1 for dimensions). For simplicity, we assume a smooth circular tube and neglect the cartilaginous rings. Martonen *et al.* (1993) study the effect of cartilaginous rings on the flow through tubes equivalent to generations 2-6 of a Weibel lung with a commercial CFD package and found that the presence of the rings had the effect of slightly narrowing the core flow of thetube. However, our interest here is in

deposition proximal to the trachea (i.e. extrathoracic deposition). The absence of cartilaginous rings in our model will not significantly affect our testing the usefulness of CFD for studying fluid flow and particle deposition in the extrathoracic airways.

The larynx has been studied more extensively to understand its role in the production of speech. Models which describe the vocal cords as a number of coupled masses (e.g. Titze, 1973, Titze, 1974) are of limited use for particle deposition as they focus on the high frequency vibrations of the vocal cords during speech production, and the propagation of that sound through the pharynx and oral cavities (also called the vocal tract). The vocal tract is often modeled as a series of cylindrical tubes (Titze uses 18) with a common axis of symmetry, which approximates the cross sectional area of the airways as measured by acoustic reflection.

More realistic models of the larynx have been developed for studying the fluid flow through, and the pressure drop across, the glottis. Scherer & Titze (1983) presented a detailed model of the larynx from which we adopted the length of the glottal opening (1.2 cm), the thickness of the glottal folds (0.29 cm), and the horizontal distance between the posterior side of the glottal opening and the posterior wall of the pharynx (1.12 cm). Brancatisano *et al.* (1983) studied the respiratory movements of the vocal cords and found that the width of the glottal opening varied during tidal breathing, with a maximum glottal width of 10.1±5.6 mm (mean ± standard error) and a maximum cross sectional area of 126±8 mm^2. For our model, we assumed the glottis was an elliptical tube with a major axis of 1.2 cm, corresponding to the anterior-posterior measurement, and a minor axis of 1.0 cm, corresponding to the transverse measurement. The cross sectional area of the larynx presented here is 95 mm^2, about half way between the maximum opening seen during inhalation, and the maximum opening seen during exhalation (70±7 mm^2). The glottis is smoothly attached to the trachea.

Observations of CT scans (n = 10) indicated that the superior tip of the epiglottis was 20 mm above the floor of the pharynx, and angled at approximately 30° to the posterior wall of the pharynx. The epiglottal folds form a tube with a diameter of approximately 1.6 cm, which smoothly joins with the glottis.

The pharynx itself is often modeled as a cylindrical tube as the anterior and posterior walls are nearly parallel. Rodenstein *et al.* (1990) found that for healthy subjects, the pharynx had an anteroposterior/transverse ratio of 0.4. Thus, for our model, we assumed the pharynx was an elliptical cylinder with the major axis (in the transverse direction) 2.5 times as large as the minor axis (in the coronal plane). The anteroposterior dimension of the airway has been measured by Lowe & Fleetham (1991), Lowe (1994), and Pae *et al.* (1994) in a total of 44 normal subjects, and the average value of 13 mm is adopted for this model. A study involving the reconstruction of the pharynx from CT scans in 85 healthy volunteers showed that in most cases, the pharynx is slightly narrower in the transverse direction near the soft palate than near the epiglottis, while the anteroposterior dimension is constant (Lowe, 1996). To account for this, the anteroposterior/transverse ratio is increased to 0.5 at the top of the pharynx. The average cross sectional area of the model pharynx is 2.98 cm^2, which compares favorably to the average value of 2.86±.34 (mean ± standard error) measured by Haponik *et al.* (1983) from CT scans.

The teeth were modeled from bite impressions (n = 5) as a semi-circle with a diameter of 25 mm, with the teeth extending back 50 mm from the lips, to a width of 45 mm at the posterior end. The upper and lower teeth were assumed to be parallel, with a 1 cm opening between them. The studies of by Lowe & Fleetham (1991), Lowe (1994), and Pae *et al.* (1994) provided the measurements to locate the roof of the mouth (a vertical

distance of 72 mm from the base of the epiglottis) and the tip of the tongue (81 mm from the base of the epiglottis) which locate the mouth relative to the larynx and pharynx.

The vault of the mouth in a coronal section is often described as a segment of a circle whose radius decreases approaching the mouth (Sorokin, 1992). Here, we have assumed that the curvature in the hard palate is constant, with a radius equal to the curvature of the front of the teeth (i.e. R=12.5 mm). The walls of the mouth are joined smoothly with the walls of the pharynx, with the exception of a small step corresponding to the tip of the soft palate. The uvula is not represented in this model.

The tongue is a large mass of muscle, and as noted above, is known to vary dramatically during the production of speech. Very little is known about the position of the tongue during normal respiration. Subjects (n = 5) were asked to hold an MDI canister (1 cm opening) between their teeth, inhale, then remove the MDI without changing the position of their jaw or tongue. It was observed that the tip of the tongue was slightly below the bottom teeth, and the top of the tongue was flat, and crossed the upper teeth approximately 3/4 of the way back. The tongue is therefore assumed to be flat in the anterior part of the mouth, beginning 5 mm below the bottom teeth, and crossing the upper teeth 40 mm from the front of the mouth. It is then smoothly joined with the anterior wall of the pharynx.

A fiberglass cast of the model was made from a hand carved wood mold. The volume of the geometry to the top of the trachea is 52 cm^3, which compares favorably with the 49 cm^3 given by the International Committee for Radiological Protection (ICRP, 1994) for the volume of the extrathoracic airways.

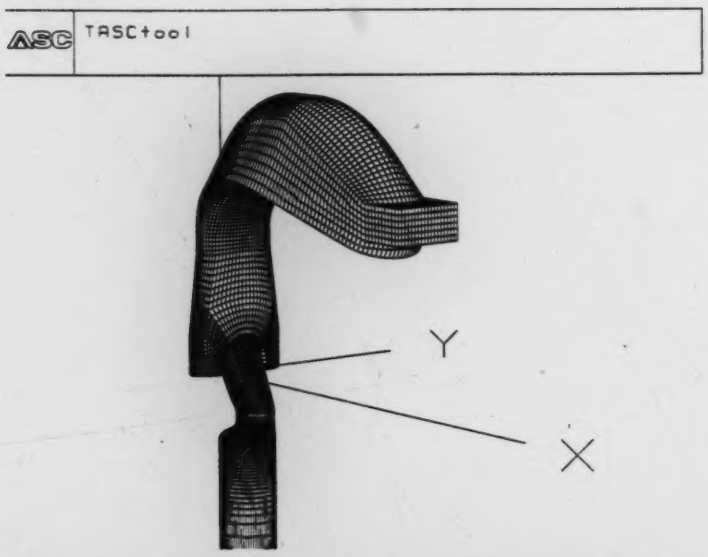

Figure 4.2. An isometric view of the physiologically realistic throat model showing the mouth, larynx, and pharyx. A square inlet is added to the front teeth. Note that the trachea has a total length of approximately 10 cm and extends out of the picture to allow for a more detialed view of the mouth and pharynx. The epiglottis is not shown in this view.

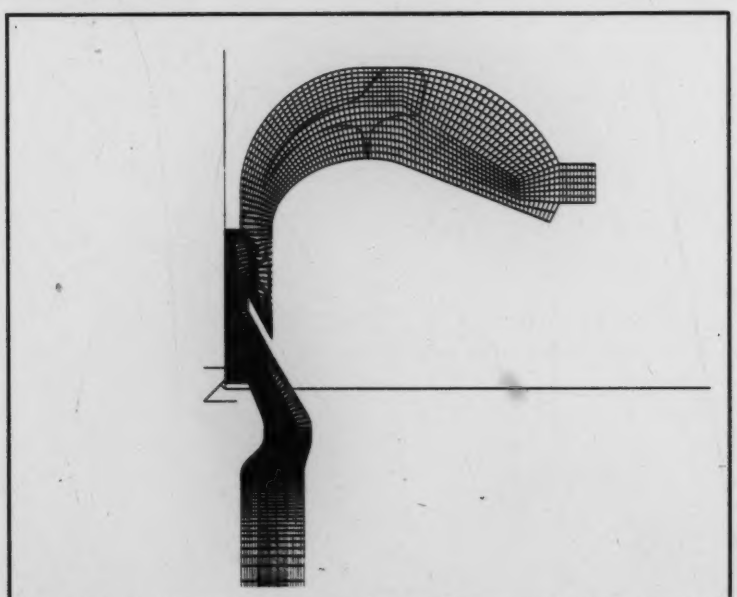

Figure 4.3: A view of the geometry through the symmetry plane showing the epiglottis and the internal structure of the model.

4.5 Particle Deposition in Bent Tubes

To validate our use of TASCflow3D, and its particle deposition predictions, it is useful to first consider a simple geometry where laminar flow is expected. The deposition of inert particles from laminar flow in bent tubes was studied experimentally by Landahl & Herman (1949), Johnston & Muir (1972) and Johnston *et al.* (1977) and computationally by Crane & Evans (1977). Additionally, theoretical equations for the deposition have been obtained (Yeh, 1974, Cheng & Wang, 1975, Diu & Yu, 1980, Balàshàzy *et al.* 1990). As the Reynolds numbers in these flows is on the order of a few hundred, TASCflow3D should have little difficulty simulating the air flow, providing a simple way of validating the use of Lagrangian particle tracking to investigate aerosol deposition

This section will first overview the geometry used in the experimental studies, and the geometry chosen for this study, along with the flow regimes and the methodology for calculating the deposition in the bend. Secondly, the grid will be described, and it will be demonstrated that the solutions obtained are independent of the grid spacing and numerical influence from the outlet boundary condition. Next, the convergence criterion will be discussed, followed by the results.

4.5.1 Geometry

Here, we have chosen a 1.5 mm diameter tube with a 19.0 mm bend radius and a 90° bend angle as studied by Johnston *et al.* (1977). Here, a 50.0 mm length of straight pipe is added to the upstream end of the bend, and a 100.0 mm length of straight pipe is added to the downstream end of the bend to ensure that numerical artifacts from the outlet boundary condition does not affect the flow in the bend.

Three regions of the tube are defined for analysis of the deposition. Region 'A' corresponds to the inlet pipe, region 'B' corresponds to the bend itself, region 'C'

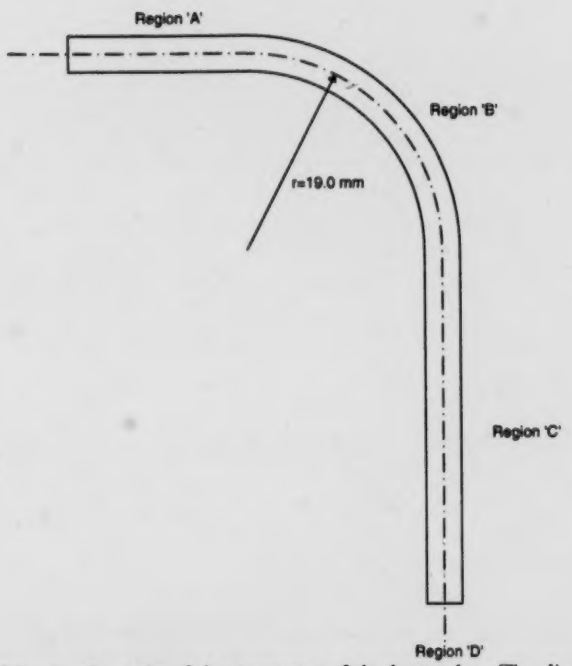

Figure 4.4. A schematic of the geometry of the bent tube. The diameter of the pipe is exaggerated for display purposes.

corresponds to the length of pipe after the bend. In addition, any particles that exit the geometry are collected on a filter, defined as region 'D'. The fractional deposition in the bend is then defined as:

$$DE = \frac{m_B}{m_A + m_B + m_C + m_D} \tag{4.10}$$

where m is the mass of particles collected in the region denoted by the subscript.

4.5.2 Grid

The base mesh used in the calculations is shown in Figure 4.5 and contains 58,695 nodes, or equivalently, 46,816 three-dimensional elements. First, it must be determined that the grid density is sufficient to resolve all the important flow features, and secondly, it must be determined that the exit boundary conditions are not influencing the results.

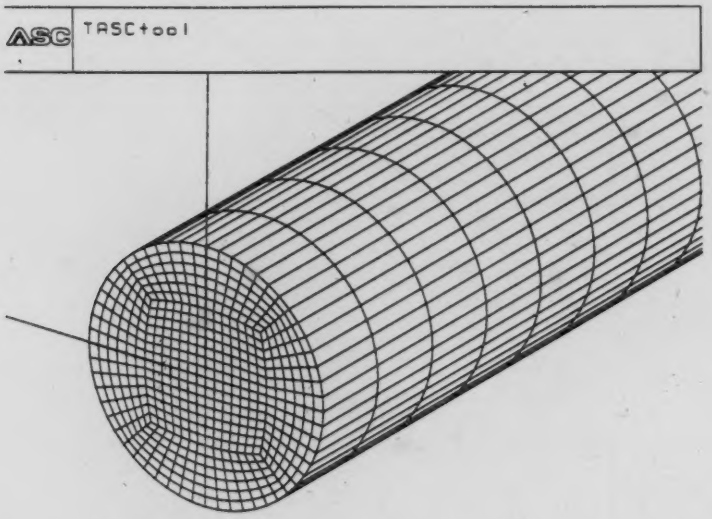

Figure 4.5. A partial view of the mesh used in the calculations showing the inlet and the mesh cross section. The large dot indicates the location of the end of the grid line used in the grid convergence studies.

The dependence of the solution on the grid density is checked for a flow rate of 0.3 liters/min. Three grid densities are used: the base grid described above, a low resolution grid with approximately twice the distance between nodes of the base grid (a total of 10,395 nodes), and a high resolution grid with approximately 1/2 the distance between the nodes of the base grid (a total of 352,175 nodes). Figure 4.6 shows the fluid speed along a gridline located approximately 1/2 of the distance between the center axis of the tube and the outside wall of the bend. The results predicted by the base grid and the high density grid are virtually identical. Figure 4.7 shows the pressure drop along the same line. Here, all three grids give similar results. It must also be determined that the exit boundary condition does not influence the solution in the region of interest. To do so, an extra 100.0 mm of tube is added to the exit pipe, and the speed and pressure drop along a grid line are

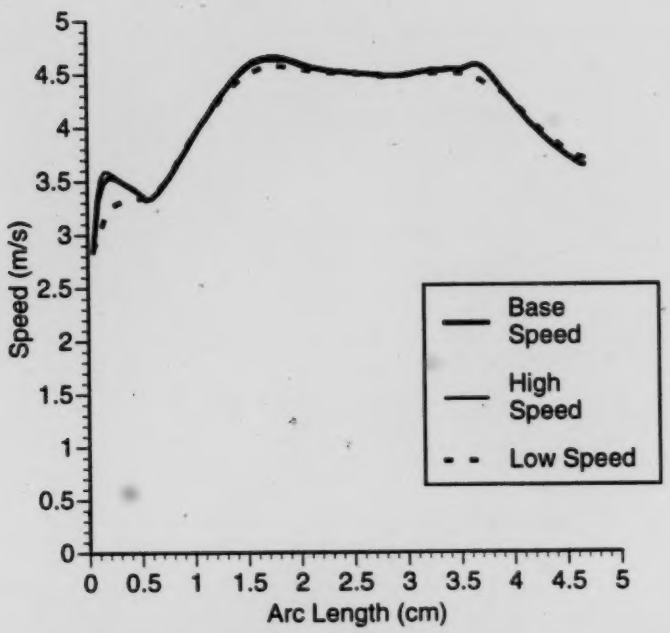

Figure 4.6. A plot of the speed of the fluid along a gridline for the three grid densities showing that the increasing the resolution of the grid beyond the base grid does not increase the accuracy of the results..

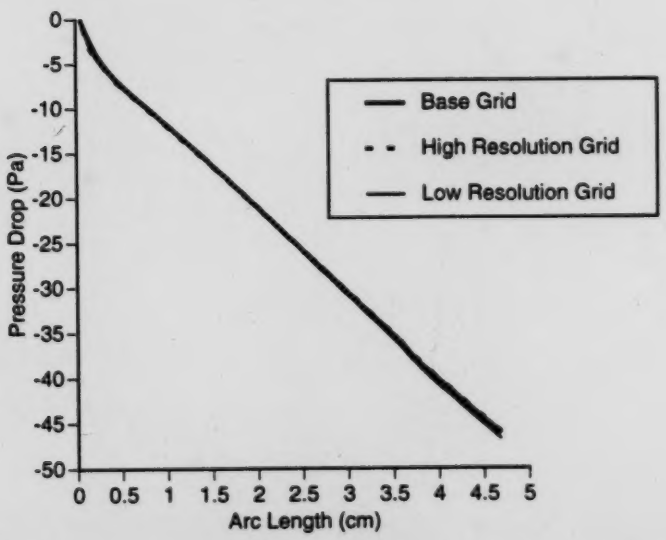

Figure 4.7. A plot of the pressure drop of the fluid along a gridline for the three grid densities showing that the increasing the resolution of the grid beyond the base grid does not increase the accuracy of the results..

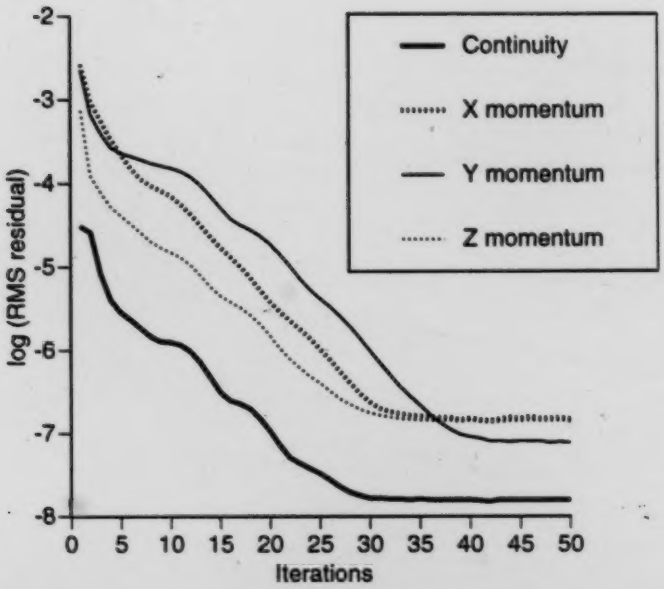

Figure 4.8. A typical plot of the dimensionless RMS residuals at each timestep for the calculations. In all cases, the maximum residuals at any grid point are less than one order of magnitude greater than the RMS value indicating that there are no local areas of high error.

compared. The difference between the two solutions is less than 0.001% at every grid point.

From the above tests, we can conclude that the solution calculated using the base grid is independent of the grid density and numerical influences from the outlet boundary conditions.

4.5.3 Convergence

Iterative convergence was achieved by allowing the code to run until there was no appreciable decrease in either the RMS value of the residual over the entire computational domain or in the maximum value of the residual at any grid point for a period of 10 iterations. Figure 4.8 shows a typical plot of the residual beginning from a uniform initial guess. Iterative convergence is achieved after approximately 40 iterations.

TASCflow3D also provides a report on the global conservation of the mass and momentum equations, an example of which is shown in Figure 4.8. The "Net Flow" gives an indication of the overall numerical accuracy of the solution. For example, the X-momentum at every grid point on the inlet boundary condition is summed (1.244×10^{-4} kg/m^2s in Figure 4.9). This is repeated for the outlet boundary condition and the wall boundary condition. The "New Flow" is the sum of these values. Since TASCflow3D solves the Navier-Stokes equations in strong conservation form using a finite volume method, there will be no artificial sources or sinks from the numerical scheme, and non-zero values of the "Net Flow" will result from round-off errors and inaccuracies due to descretization and the finite differencing scheme. The "Net Flow", should be negligible with respect to the values at the boundary conditions to ensure an accurate solution. In this example, the "Net Flow" in the X and Y momentum is approximately 6 orders of magnitude lower than the boundary condition values, and the "Net Flow" for mass conservation are approximately 7 orders of magnitude less than the boundary conditions values. In the case of the Z momentum, the net flow is a much smaller fraction of the values at the boundaries, but in this case, the only source of Z momentum is the secondary

Momentum and Mass Flow Summary

Boundary or source	X-momentum	Y-momentum	Z-momentum	Mass
B.C. # 1, WALL	-1.231E-04	-1.428E-04	4.061E-07	0.000E+00
B.C. # 2, OUTFLOW	-1.309E-06	1.428E-04	-4.046E-07	-1.548E-05
B.C. # 3, INFLOW	1.244E-04	2.963E-11	-7.071E-11	1.548E-05
Net Flow	-8.731E-11	4.953E-10	1.480E-09	-1.819E-12

Figure 4.9. A summary table of the mass flows from the same run shown in Figure 4.8. It can be seen that the net flow is approximately 5 orders of magnitude lower than the average values on the boundaries for X and Y momentum and conservation of mass.

flows generated as the air passes through the bends, which is small compared to the momentum in the X and Y directions. By considering both the iterative convergence and the mass flow summary, we can determine that the solutions are converged.
For all the results presented in Section 4.5, the value in the RMS residuals over the entire flow field is always less than $2x10^{-7}$. The "Net Flow" in the conservation of X and Y momentum are approximately 5 orders of magnitude less than the values at the boundaries.

4.5.4 Results

Once it was determined that a converged solution was obtained which was independent of the grid density, particles were injected in the flow, and their paths calculated. A total of 100,000 particles were injected at random locations across the inlet boundary of the tube. In the CFD calculations, a monodisperse aerosol of uranine particles having a diameter of 5.0 μm and density 1.3 g/cm^3 was assumed, similar to the particles used experimentally by Johnston *et al.* (1977). In Figuire 4.10, our deposition probabilities calculated by CFD are compared with the experimental values of Johnston & Muir (1973) and Johnston *et al.* (1977), the computational results of Crane & Evans (1977), and the theoretical expression of Balàshàzy *et al.* (1990) for the inertial deposition in a bent tube. The CFD results presented here agree well with the available experimental data. Deposition patterns were not presented in the experimental studies, so comparisons of the deposition patterns are not possible.

In the above calculation, a uniform inlet velocity profile was used. When a parabolic inlet velocity profile was used, the differences in the deposition probabilities were less than 1% from those calculated with a uniform profile. Most theoretical investigations show a slight increase in the deposition efficiencies when a parabolic entrance profile is used. This departure from the theoretical predictions is the result of our long entrance tube

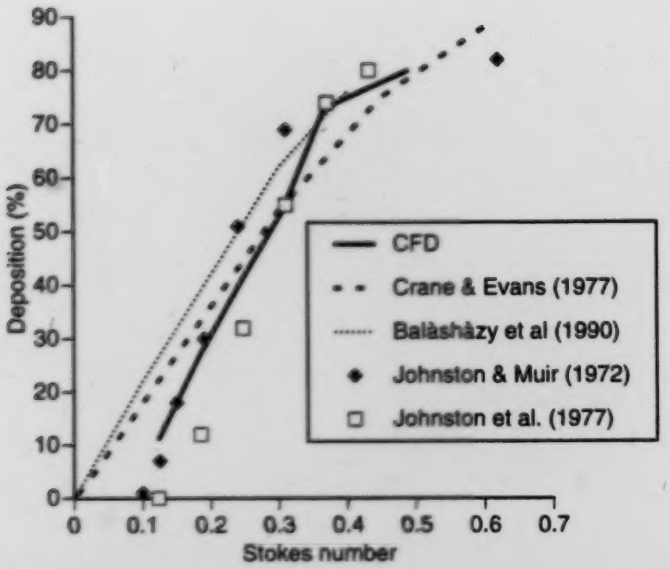

Figure 4.10. The calculated deposition in a tube with a 90° bend compared to experimental, theoretical, and other computational results. The results all show good agreement.

of approximately 30 tube diameters allowing the flow to develop before the bend is encountered.

From the results of this section, we can conclude that the Lagrangian particle tracking as implemented in TASCflow3D accurately reproduces the experimental deposition of aerosols in geometries where the flow is laminar and easily determined numerically.

4.6 Deposition in the USP model throat.

The second geometry studied is similar to the model throat described by the United States Pharmacopeia (1995) and will be referred to in this thesis at the USP model throat. The USP model throat is designed to be attached to the inlet of a cascade impactor, or a single stage impactor (described by USP 1995), to simulate the filtering capabilities of the

extrathoracic region of the respiratory tract. Here, we study this geometry because it provides an intermediate step between the simple geometry and flow of the bent tubes, and the complex geometry and flow of the physiologically realistic model throat.

4.6.1 Geometry and Grid

Fabrication instructions for this model are given in the USP (1995). In brief, the USP model throat consists of a 4.5 cm diameter sphere with a 2.9 cm diameter inlet tube with length 3.5 cm, and a 2.0 cm diameter outlet tube with length 2.0 cm oriented 90° from the inlet tube. On the inlet tube is a ground glass socket (female) to accept an adapter for the mouthpiece of the DPI or MDI being tested. The geometry studied here includes the inside surface of the ground glass socket. The outlet tube has a male ground glass socket to attach the impinger model throat to either a liquid impinger, or a cascade impactor. The geometry studied here includes the inside surface of the socket.

As was briefly mentioned in Section 4.3, generating a grid for the USP model throat requires consideration of both the flow and the turbulence model. Not only must the nodes be placed to resolve the flow features, but there must be enough nodes near the wall to resolve the damping functions used in the turbulence model. Figure 4.11 shows the base grid used in the calculations where it intersects the outside surface. Figure 4.12 shows the grid on the symmetry plane. It can be seen in both Figures 4.11 and 4.12 that the grid is much more dense near the walls, and near any sharp bends in the geometry.

This grid was created in an iterative manner. First, a solution was obtained on a uniform grid. The grid was refined wherever the maximum residual at a grid point was more than one order of magnitude greater than the RMS value of the residual, and the grid was resolved near the walls to obtain the necessary resolution for the damping functions. This process was repeated until an acceptable solution was obtained. The grid was then

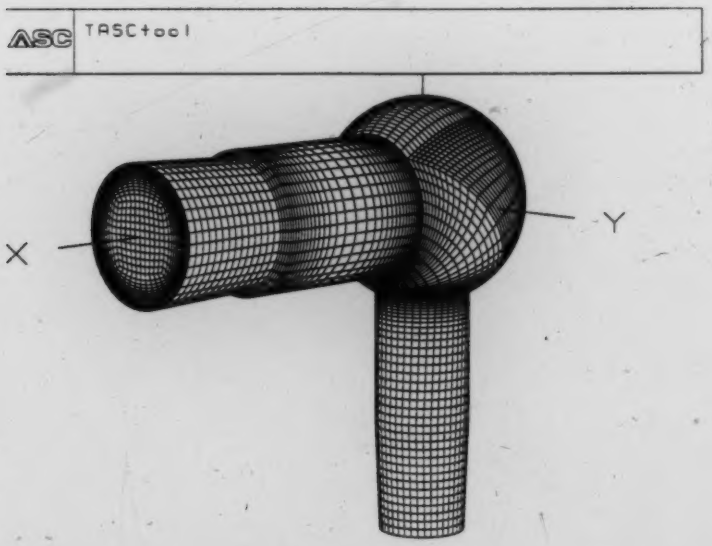

Figure 4.11. A view of the mesh for the USP model throat. The flow enters parallel to the X-axis, and exits at the bottom.

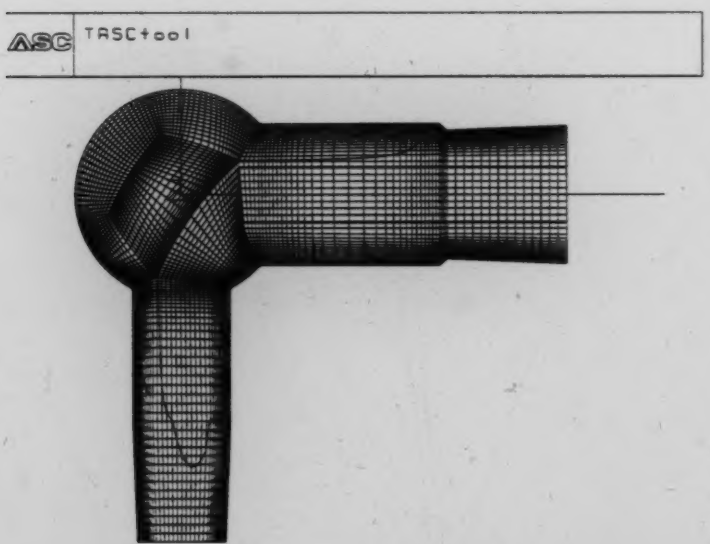

Figure 4.12. The grid for the USP model throat through the symmetry plane. The thick line gives the approximate location of the grid line used in the grid convergence studies.

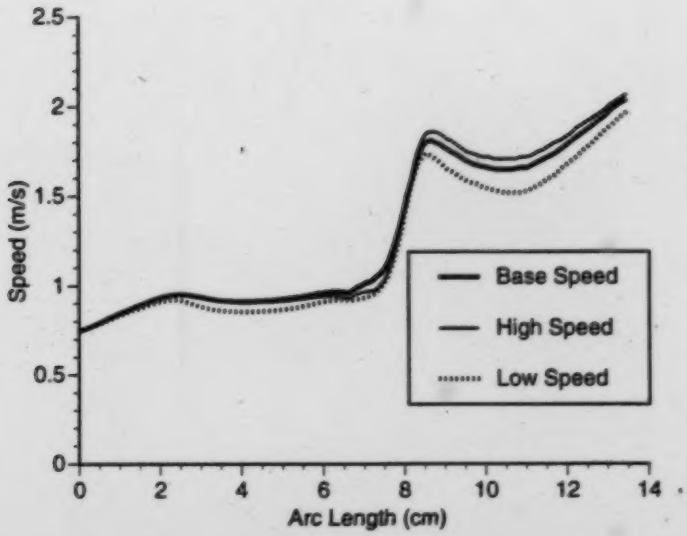

Figure 4.13. A plot of the speed of the fluid along a gridline for three grid resolutions of the USP model throat showing that increasing the resolution of the grid beyond the base grid results in only a slight increase in accuracy (<1% at all points).

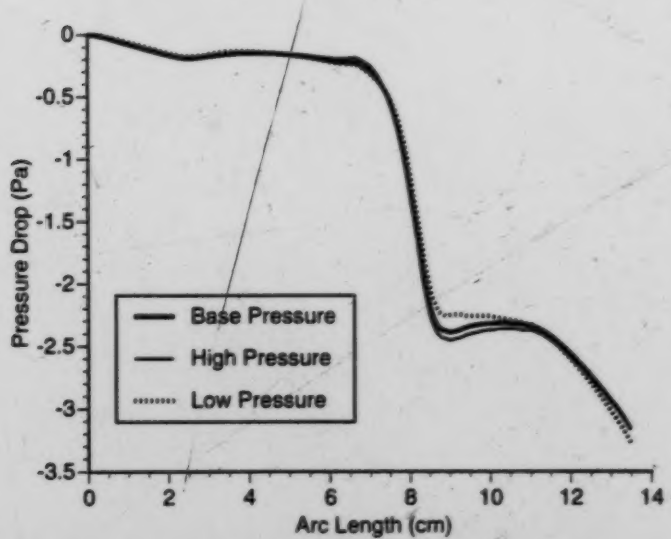

Figure 4.14. A plot of the pressure drop of the fluid along a gridline for three grid resolutions of the USP model throat showing that increasing the resolution of the grid beyond the base grid results in only a slight increase in accuracy (<1% at all points).

checked for grid convergence by increasing the spacing between the nodes by 50% in each direction to create a low resolution grid, and by decreasing the spacing between the nodes by 50% in each direction to obtain a high resolution grid. Figure 4.13 shows the fluid speed along a grid line, and the pressure drop is shown in Figure 4.14. From these results we can see that the base grid with 129,645 nodes is sufficiently resolved.

The final check on the grid is to ensure that the exit boundary condition does not influence the flow. An additional 10 cm of tube was added to the exit boundary condition, and it was found that both the velocity and pressure drop along a grid line differed by less than 0.05% at every grid point.

4.6.2 Boundary conditions

The airflow entering the model was assumed to be plug flow. To determine the value of the turbulence intensity at the inlet, the output of a Pari LC+ nebulizer was measured at a flow rate of 28.3 l/min (6.0 l/min from the compressor, and 22.3 l/min through the vent). The velocity distribution of aerosol droplets leaving the nebulizer was determined with a phase Doppler anemometer. Dividing the RMS value of the droplet velocity by the mean velocity exiting the nebulizer provided a turbulence intensity of 0.12 which is used as the inlet turbulence intensity for the calculations. The turbulence length scale is assumed to be 1/10 of the diameter of the inlet tube. The inlet turbulence length scale was varied 1/30 of the inlet tube diameter to 1/2 of the inlet tube diameter with no noticeable effect on the solution.

4.6.3 Convergence

Iterative convergence was achieved when the RMS residuals were all less than 4×10^{-6}. The maximum residual at any node was less than 3×10^{-5} showing that there are no local areas of high error on the grid. Additionally, Figure 4.15 shows that the "Net Flow"

Momentum and Mass Flow Summary

Boundary or source	X-momentum	Y-momentum	Z-momentum	Mass
B.C. # 1, WALL	2.364E-03	-1.068E-03	1.113E-06	0.000E+00
B.C. # 2, INFLOW	-2.355E-03	8.563E-09	1.714E-09	5.478E-04
B.C. # 3, OUTFLOW	-9.536E-06	1.068E-03	-1.251E-06	-5.478E-04
Net Flow	-4.020E-07	1.377E-07	-1.357E-07	-2.212E-09

Figure 4.15. Mass flow summary for the flow solution on the base grid used in the particle tracking calculations. The "Net Flow" in the X-momentum and Y-momentum is approximately 4 orders of magnitude less than the boundary values, and the "Net Flow" in continuity approximately 5 orders of magnitude lower than the boundary values

in the conservation of X and Y momentum is approximately 4 orders of magnitude less than the values at the boundaries.

4.6.4 Experimental studies of aerosol deposition in the USP model throat

To validate the computational results, a wooden model of the USP throat geometry was built and used as a form for a fiberglass model. A Pari LC+ nebulizer was attached to the inlet of the USP model throat via heat-shrink tubing. The outlet was attached directly to a Marquest filter and a vacuum pump calibrated to draw 28.3 l/min of air through the apparatus. Figure 4.16 shows a schematic of the experimental setup. Normal saline solution (0.9% NaCl by weight) tagged with albutum colloid suspension is nebulized. The size of the aerosol produced by the specific nebulizer used in this study was measured to have an MMD of 4.8 μm and a GSD of 1.65 with a Dantek PDA system.

To ensure the validity of our assumption of inert particles in the CFD calculations, it is important to investigate the stability of the droplets exiting the nebulizer. The stability of the aerosol was determined by calculating the growth of the droplets through the nebulizer as described in Section 3.5, and it was found that more than 95% of the aerosol

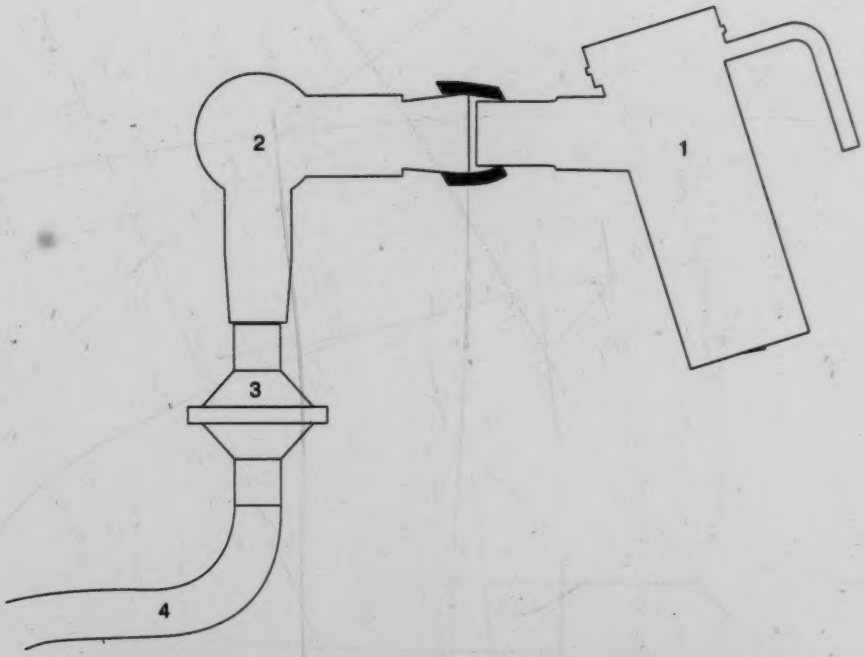

Figure 4.16. A schematic of the experimental setup used to determine the deposition of radiolabelled aerosols in the USP throat model. The nebulizer (1) is attached to the USP throat model (2) via heat-shrink tubing. Aerosol passing through the model is collected on a filter (3) attached to a vacuum pump via hosing (4).

was in equilibrium at the exit of the nebulizer. Additionally, Stapleton & Finlay (1997) showed that aqueous droplets produced by nebulizers can change size significantly when their size is measured by a cascade impactor due to heat transfer from the cascade impactor to the aerosol. It is useful to consider if this effect is important here.

To estimate an upper bound for the temperature drop of the fluid as it passes through the model, we will consider a straight tube with a diameter of 3.0 cm and a length of 10 cm, so that the diameter and volume of the test tube are close to the diameter of the inlet and exit tubes and the total volume of the USP model throat. (Note that this analysis is also applicable to the phydiologically realistic throat model described in Section 4.7. because it has a similar volume and droplet residence time.) The equation for the increase in the bulk temperature of a fluid flowing through a tube is

$$\frac{T_\infty - T_{m,o}}{T_\infty - T_{m,i}} = \exp\left(\frac{-PL}{\dot{m}C_p}\overline{U}\right) \tag{4.11}$$

where T_∞ = ambient temperature outside the pipe
$T_{m,i}$ = mean temperature of the fluid in the pipe at the pipe inlet
$T_{m,o}$ = mean temperature of the fluid in the pipe at the pipe outlet
P = pipe circumference
L = pipe length
$\dot{m}$ = mass flow rate through the pipe
$\overline{U}$ = average resistance to heat transfer

The only unknown on the right hand side of the equation is $\overline{U}$. To calculate a value for $\overline{U}$ we first consider that the Nusselt number for steady laminar flow is 3.66. Using the heat conductance of water and the diameter of the pipe, a value for the convective heat transfer coefficient h can be calculated to be h=5.0. Then we can write (Incropera & DeWitt, 1990):

$$\overline{U} = \frac{1}{\frac{1}{h} + \frac{r_1}{\kappa}\ln\left(\frac{r_2}{r_1}\right)} \approx 5 \tag{4.12}$$

where r_1 and r_2 are the inner and outer radii of the tube, and κ is the heat transfer coefficient of the tube (fibreglass). Substituting into Equation (4.7), the maximum temperature drop is on the order of 0.4°C. Five micrometre droplets of isotonic saline exposed to this temperature difference would need to change their size by less than 1% to come into equilibirum with the new temperature. It can therefore be assumed that the droplets do not change size as they move through the model.

The aerosol was drawn through the model for 60 seconds, after which the model and filter were imaged by a Picker Prism 2000 gamma camera for 300 seconds. The fraction of aerosol depositing in the model was determined by counting the photons emitted by:

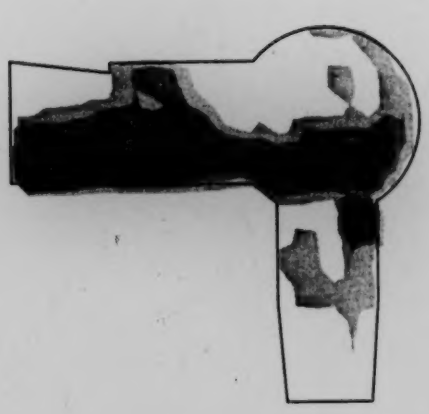

Figure 4.17. A greyscale image of the deposition of radiolabelled aerosol in the USP model throat. Air enters on the left, and exits on the bottom. The darker areas correspond to areas of higher deposition.

$$DE = \frac{C_m}{C_m + C_f} \tag{4.13}$$

where C_m is the number of counts from the model, and C_f is the number of counts on the filter. From Equation (4.10), 5.9% of the aerosol mass entering the USP model throat deposits on the walls.

The gamma camera image of the model shown in Figure 4.17 gives information on the deposition pattern in the model. It can be seen that there is significant deposition in the entrance tube, particularly in the region immediately downstream of the area corresponding to the ground glass inlet cone. In the spherical section of the USP throat model, most of the deposition occurs in a ring around the intersection with the exit tube. There is some deposition on the back of the sphere (i.e. on the side opposite to the inlet). There is minimal deposition in the exit tube, with most of it occurring on the back of the tube near the top.

4.6.5 Results

The flow in the USP model throat is complex, and highly three dimensional. The characteristics of the flow can be viewed by considering the tracks of massless particles injected in the flow. Figure 4.18 shows tracks from a side view, and shows the large recirculating regions in the spherical elbow. Aerosol enters from the right, and exits at the bottom. Figure 4.19 shows two vortical patterns that form in the sphere that are convected through the outlet tube.

Although the flow patterns in the USP model throat are interesting, here, we are primarily interested in the particle deposition. The particle deposition in this geometry was calculated using CFD for a monodisperse aerosol with a size equal to the measured MMD of the nebulizer. Additionally, the deposition for a polydisperse distribution with an MMD and GSD equal to that produced by the nebulizer was used.

Table 4.1 gives the quantitative results of the CFD particle calculations. The total deposition predicted by the CFD is approximately twice that seen in the experimental studies.

	Experimental Values	Monodisperse Aerosol	Aerosol Distribution
Inlet		0.3%	0.6%
Sphere		7.5%	8.0%
Outlet		3.6%	4.0%
Total	5.9%	11.4%	12.6%

Table 4.1. Calculated total deposition in the USP throat model showing the effect of using a monodisperse *vs.* a polydisperse aerosol. All values are a percentage of total mass of aerosol entering.

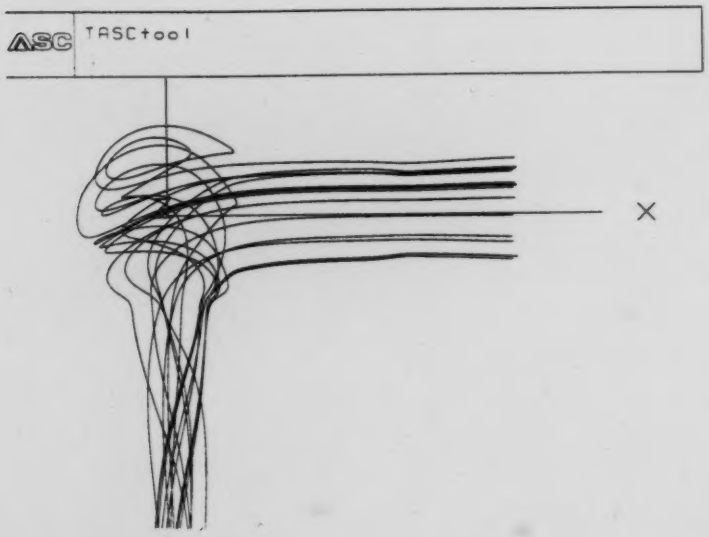

Figure 4.18. Tracks of massless particles in the USP model throat viewed from the side of the model. The flow enters from the right, and exits out the bottom.

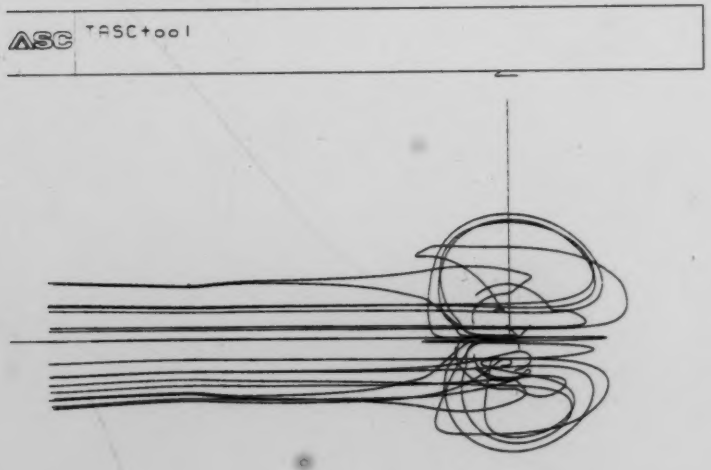

Figure 4.19. Tracks of massless particles in the USP model throat viewed from the top of the model. The flow enters from the left, and exits into the page.

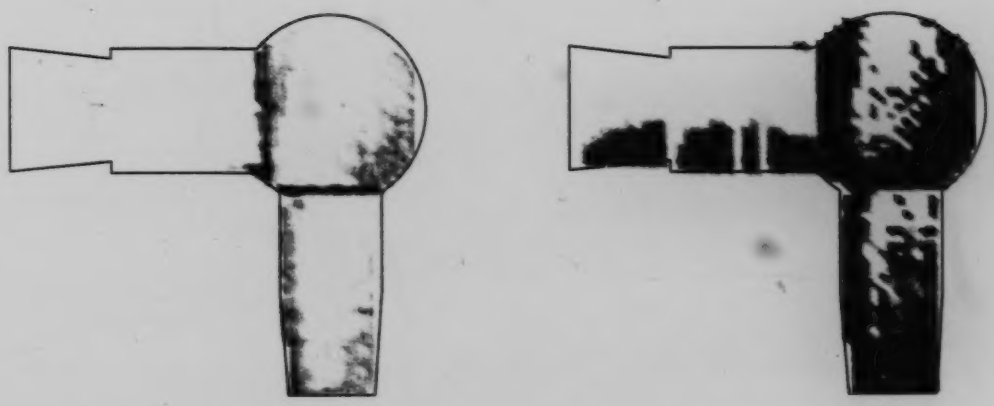

Figure 4.20. Calculated deposition patterns for the USP model throat. (a) shows the pattern for a monodisperse aerosol equal to the MMD of the aerosol produced by the nebulizer used in the experimental tests. (b) shows the calculated deposition pattern for a polydisperse aerosol with and MMD and GSD equivalent to the aerosol produced by the nebulizer.

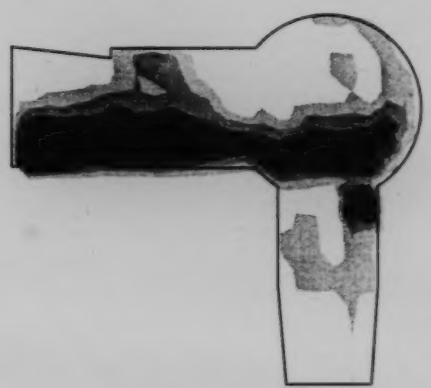

Figure 4.21. Experimental deposition in the USP model throat. This figure uses the same data as Figure 4.17 and is shown here for comparison purposes.

Figures 4.20 (a) and 4.20 (b) show the deposition pattern predicted by the CFD. Figure 4.17 is repeated here (as Figure 4.21) for comparison purposes. In the experimental results shown in Figure 4.22, most of the deposition occurs on the bottom of the inlet tube. In the computational results, most of the aerosol deposits in a narrow ring around where

the outlet tube intersects the sphere, with very little aerosol depositing in the inlet tube (this can also be seen in Table 4.1).

4.7 Aerosol deposition in the physiologically realistic throat model

4.7.1 Geometry and grid

The third geometry studied is the physiologically realistic throat model described in Section 4.4. The geometry contains many features that can be expected to complicate the flow calculations. For example, recirculation regions can be expected in the cavernous roof of the mouth, below the soft palate, and distal to the larynx.

The geometry was gridded with 63 blocks, and the base grid contains approximately 230,000 nodes. The surface grid is partially shown in Figure 4.2, and a cross section of the base grid through the symmetry plane is shown in Figure 4.22.

Two distinct areas of the grid can be identified. The first consists of regions where the flow impinges on a wall (e.g. on the posterior wall of the roof of the mouth, and on the inferior end of the pharynx) or where the flow recirculates (e.g. the roof of the mouth, posterior wall of the pharynx). In these areas, the law of the wall is not expected to be valid. The design of the base grid placed first grid point at $y^+ \leq 10$ in some of these regions, but because the law of the wall is not valid, this is acceptable. In regions where a reasonable approximation of boundary layer flow can be expected, for example on the tongue or in the trachea, the first grid point is at $y^+ \geq 25$. A standard $k-\varepsilon$ turbulence model with wall functions was used.

Grid convergence was determined by comparing the base grid with a low resolution grid with approximately 60,000 nodes, and with a high resolution grid with

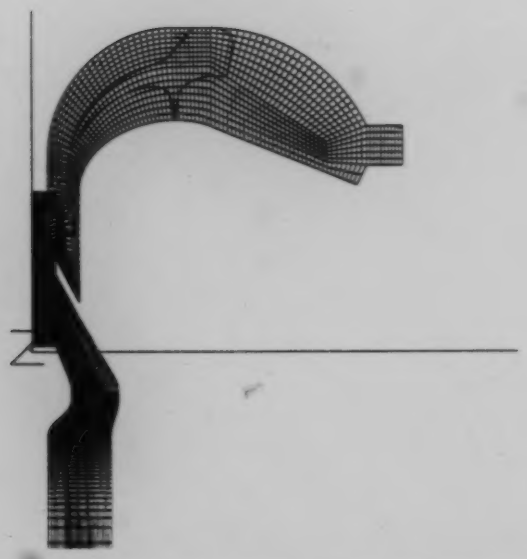

Figure 4.22. A cross sectional view of the base grid for the physiologically realistic throat model. The red lines indicate the approximate location of the grid lines used in the grid convergence studies.

approximately 600,000 nodes, representing a decrease and increase of approximately 50% in the nodal density respectively. Because of the complexity of the grid, it was difficult to find a continuous grid line through the entire flow field to use for the grid convergencestudies. Instead, two separate lines are studied, the first begins in the mouthpiece, and passes through the mouth and pharynx and terminates on the superior surface of the epiglottis, and the second begins at the posterior wall of the pharynx and runs through the larynx and trachea. The approximate location of the lines are shown in Figure 4.22. Figures 4.23 and 4.24 compare the speed and pressure drop along the grid lines for the three grids, and it can be seen that the increase in accuracy of the high resolution grid is minimal.

4.7.2 Boundary conditions

The inlet boundary conditions used for this model are the same as for the USP model throat: plug velocity profile for 28.3 l/min, turbulence intensity of 0.12, and a turbulence length scale of 0.003 m. As with the USP model throat, the turbulence length scale was varied between 0.001 m and 0.01 m with no noticeable effect on the results. Decreasing the turbulence intensity also had little effect on the results, and all attempts to obtain converged solutions at higher turbulence intensities were unsuccessful.

4.7.3 Convergence

Iterative convergence was achieved when the RMS residuals over the entire flow field were all less than 7×10^{-8}. The maximum residual at any node was less than 2×10^{-6} indicating that there may be some areas of high error. Here, the maximum residuals are in a small recirculation region distal to the larynx on the posterior wall of the trachea. Most particles pass through this region close to the anterior wall of the trachea, so the impact of this error can be expected to be small.

The 'New Flow' summary is shown in Figure 4.25. Here it can be seen that in spite of the small RMS errors, the "Net Flow" is only 4 orders of magnitude less than the values at the boundaries.

Momentum and Mass Flow Summary

Boundary or source	X-momentum	Y-momentum	Z-momentum	Mass
B.C. # 1, WALL	1.373E-03	3.229E-03	3.255E-07	0.000E+00
B.C. # 2, INFLOW	-1.378E-03	-1.352E-08	3.458E-10	5.480E-04
B.C. # 3, OUTFLOW	4.612E-06	-3.229E-03	-3.321E-07	-5.480E-04
Net Flow	-4.334E-07	-4.843E-08	-6.280E-09	1.572E-09

Figure 4.23. A summary table of the mass flows for the converged solution on the base grid used for the particle deposition calculations.

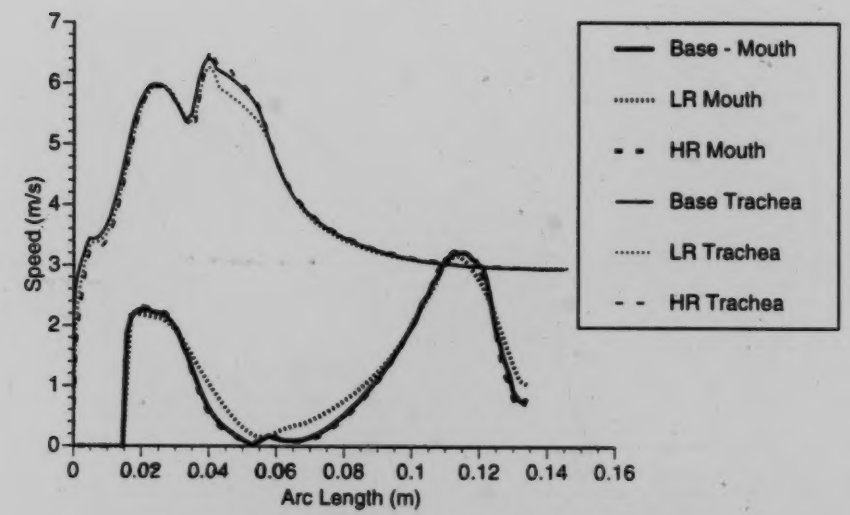

Figure 4.24. A plot of the speed of the fluid along the two grid lines for the three grid densities showing that increasing the grid resolution beyond the base grid does not increase the accuracy of the results. LR=low resolution. HR=high resolution.

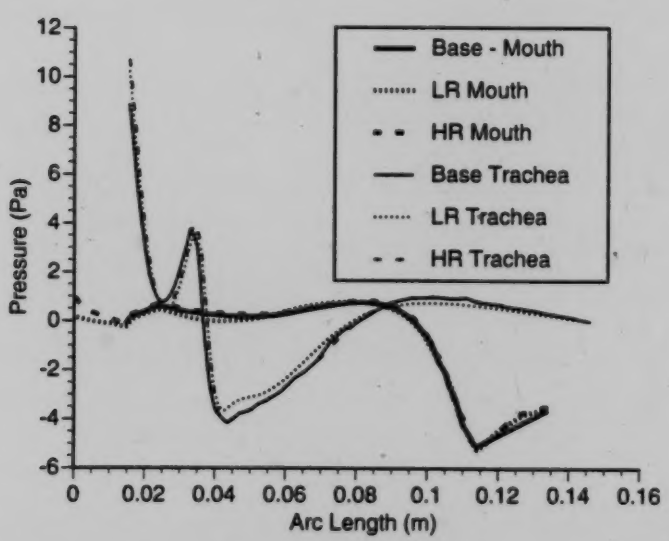

Figure 4.25. A plot of the pressure drop in the fluid along the two grid lines for the three grid densities showing that increasing the grid resolution beyond the base grid does not increase the accuracy of the results. LR=low resolution. HR=high resolution

Figure 4.26. A greyscale image of the deposition of radiolabelled aerosol in the mouth and pharynx of the model throat. The deposition mainly occurs on the surface of the tongue and the bottom of the pharynx.

4.7.4 Experimental studies of aerosol deposition in the physiologically realistic throat model

A hand carved wooden model of the throat geometry was built and used as a form for a fiberglass model. The throat model was tested using the same technique as the USP model throat described in Section 4.6.4, and from Equation (4.10), it was determined that 21% of the mass entering the mouthpiece deposited on the walls of the model.

The pattern of deposition is shown in Figures 4.26 and 4.27. Approximately 30% of the aerosol which deposited in the model landed in the mouth, mainly on the tongue; 21% of the aerosol landed in the pharynx, with the most significant deposition on the inferior wall of the pharynx; and the remaining 49% deposited in the larynx (deposition on the superior surface of the epiglottis is considered part of the trachea).

The empirical equations given earlier in this thesis for deposition in the extrathoracic region of the respiratory tract provide a verification on both the experimental and computational results as they represent average values of extrathoracic deposition in actual subjects. Assuming a monodisperse aerosol with a particle diameter of 4.8μm, a

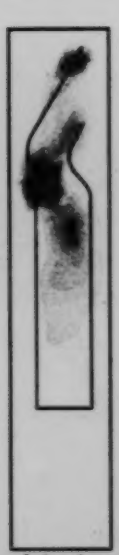

Figure 4.27. A greyscale image of the deposition of radiolabelled aerosol in the larynx and trachea. The dark spot corresponds to the larynx. Significant deposition is also observed on the superior surface of the epiglottis.

flow rate of 28.3 l/min, and a tidal volume of 1 liter, a deposition fraction of 18.4% can be calculated with Equation (2.21). For a polydisperse aerosol with an MMD=4.8 and GSD=1.65, Equation (2.21) predicts that 25.6% of the aerosol should deposit.

4.7.5 Results

The deposition in the physiologically realistic throat was calculated using the same aerosols used with the USP model throat: a monodisperse aerosol with a diameter equal to the MMD of the aerosol produced by the nebulizer used in the experimental studies (4.8 ?m) and a polydisperse aerosol with and MMD and GSD equal to the values measured for the aerosol produced by the nebulizer used in the experimental studies (MMD of . 4.8 ?m, and a GSD of 1.7).

The deposition as a percentage of the mass entering the mouthpiece is given in Table 4.2. In the previous section, it was noted that the average value of the extrathoracic deposition expected in actual subjects predicted by Equation (2.21) for a polydisperse

Region	Experimental Values	Monodisperse Aerosol	Polydisperse Aerosol
Mouth	6.4%	10.3%	20.0%
Pharynx	4.0%	8.9%	15.0%
Larynx/Trachea	7.6%	28.0%	29.8%
Total	21%	47.2%	64.8%

Table 4.2. Calculated total and regional deposition in the physiologically realistic throat model showing the effect of using a monodisperse *vs.* a polydisperse aerosol. All values are a percentage of total mass of aerosol entering.

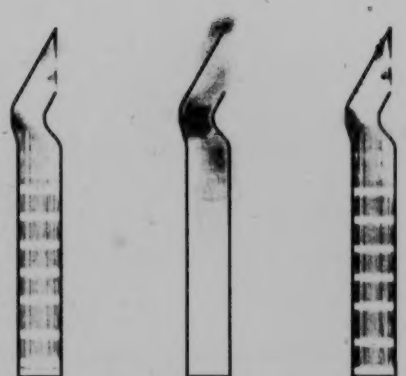

Figure 4.28. Calculated deposition pattern for the physiologically realistic throat model compared with the experimental results. (a) shows the deposition pattern in the trachea calculated using the monodisperse aerosol, (b) shows the experimental results (same data as Figure 4.27), and (c) .shows the deposition pattern calculated using the polydisperse aerosol.

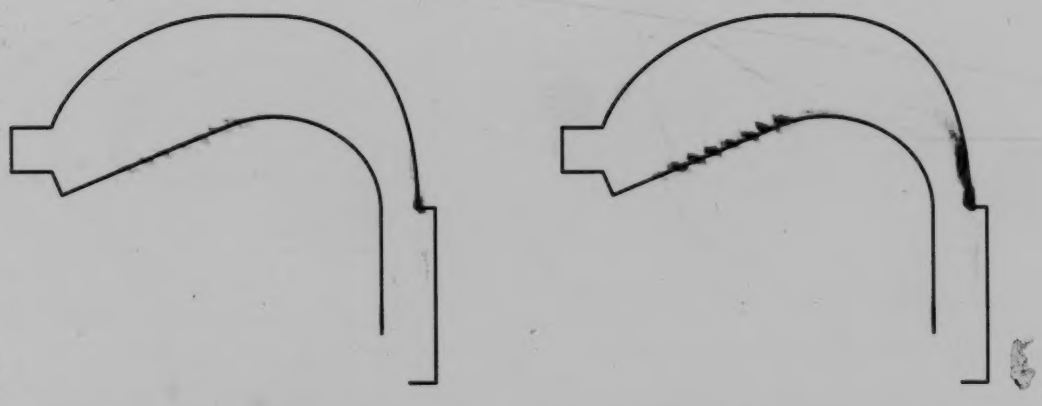

Figure 4.29. Calculated deposition pattern for the physiologically realistic throat model compared with the experimental results. (a) shows the deposition pattern calculated using the monodisperse aerosol, (b) shows the deposition pattern calculated using the polydisperse aerosol

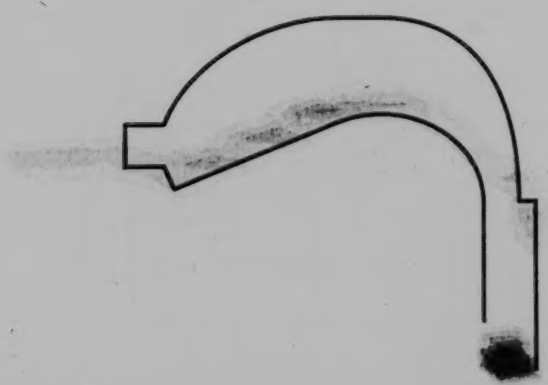

Figure 4.30. Experimental results of deposition in the mouth and pharynx. Same as Figure 4.26

aerosol (25%) is close to the experimentally determined deposition in the model (21%). As was seen with the USP model throat, the calculated deposition is approximately twice the experimental value.

However, the deposition pattern predicted predicted by the CFD is reasonably close to the experimentally observed pattern. Figures 4.29 4.30 compare the experimentally

determined deposition in the larynx/trachea with the computational results. It can be seen that the results for a polydisperse aerosol show reasonable agreement with the experimental patterns, with the most notable exception being that the CFD does not predict as much deposition on the bottom of the pharynx as was observed experimentally.

5. Conclusions

This manuscript has dealt with many of the issues involved in the study of drug delivery to the respiratory tract. Chapter 2 dealt with the development of a model that predicts the probability of a particle or droplet depositing in the different regions of the respiratory tract. Deposition due to sedimentation and diffusion are calculated from theoretical expressions for aerosol deposition in a system of randomly oriented tubes. Inertial impaction is calculated by an empirical expression matching the deposition in lung casts. Extrathoracic deposition is also calculated by an empirical expression.

The model also calculates the growth of droplets in response to their environment, and it was shown that one must consider not only the effect of their environment on the aerosol droplets, but also the effect of the aerosol droplets on their environment.

Here we have chosen to apply the deposition model to therapeutic aerosols generated by medical nebulizers, but in principle, it could be used for predicting the deposition of other devices, or in other applications. Indeed, a significant portion of the research in this area is supported by the occupational health and safety industry who are interested in the effects of human exposure to hazardous aerosol environments.

Chapter 3 characterized the output of medical nebulizers, and showed how this data can be used in conjunction with a deposition model to predict the actual dosage of medication delivered to the respiratory tract.

In developing a methodology for testing nebulizers so that a hygroscopic deposition model could be used to predict the pulmonary deposition, it was found that there are many factors that influence the drug delivered to the respiratory tract such as the droplet distribution, droplet number density, nebulizer mass output rate, ambient humidity and temperature, initial volume fill, initial solution concentration, and the design of the nebulizer itself (i.e. vented or unvented). To properly compare the output of nebulizers, all of these factors must be recorded or the value of the comparison is diminished. The method presented here accounts for all of these factors, and combines it with a sophisticated pulmonary deposition model to provide an estimate of the effectiveness of the nebulizer when used in a clinical setting.

The natural extension for this work is to develop a methodology for predicting the deposition of drugs formulated as suspensions, and drugs delivered by MDIs and DPIs. In both these cases, a major challenge will lie in measuring the output of the device correctly.

Overcoming the deficiencies in the deposition model presented here will most likely not be possible without a major shift in the current approach. One such approach is to use computational fluid dynamics (CFD). CFD has many attractive attributes, and is becoming increasingly accessible as a tool for researchers outside of traditional engineering areas.

Chapter 4 of this manuscript dealt with many of the issues involved in using CFD in the respiratory tract. A commercial code was tested on a variety of flows to investigate the usefulness of 'standard' CFD techniques for studying the flow and particle deposition in the respiratory tract. First, the particle deposition in tubes with simple 90° bends was studied, and it was found that the results duplicated both experimental the theoretical results available in the archival literature.

Next, a geometry similar to the USP model throat was investigated computationally and experimentally. Here, CFD did not perform well. The calculated filtering efficiencies were approximately twice the experimentally determined values. Further, the deposition pattern was not in close agreement. In the experimental results, the majority of the deposition occured in the inlet tube, while the CFD predicted that most of the deposition would occur in a small ring where the exit tube joins the spherical elbow.

Finally, a novel throat model was described which closely approximated the shape of actual extrathoracic airways. The experimentally determined filtering efficiency of the model was similar to the deposition seen in actual throats. Again the filtering efficiencies calculated by the CFD were approximately twice the experimentally determined value. Here, the calculated deposition pattern more closely resembled the experimentally determined value with the exception that the CFD predicted less deposition on the bottom of the pharynx than was seen experimentally.

The reasons for the poor performance of the CFD are unclear. Since the predictions from the simple bent pipes with laminar flow show good agreement with experimental data, the turbulence model, and the implementation of turublent dispersion are suspect.

Turbulence modeling is a complex subject, owing to its random nature, yet there is enough structure to turbulence that purely stochastic models do not perform well. Turbulence models perform adequately in flows for which they have been calibrated, mainly high Reynolds number and boundary layer flows. As was mentioned in Section 4.1, the flows seen in the USP model throat and the physologically realistic throat have many characteristics (e.g. curved streamlines and recirculation regions) that are known to cause one and two-equation turbulence models to preform poorly. This may cause errors

in the mean streamlines. Additionally, it is unclear how particles themselves will affect the turbulence. Here, it is assumed that the particles do not affect the turbulence.

A Lagrangian trajectory model is used here to track particles through the turbulent field. The effect of turbulence on the particle tracks is modeled using an eddy lifetime model with the eddy characteristics calculated from the local turbulence quantities. This approach has a number of difficulties. First, the calculated turbulent field is approximate (and may be in error due to the turbulence model), and turbulent fluctuations chosen by Equation (4.3) will not satisfy the continuity equation for velocity fluctuations, hence, the flow field used in the particle trajectory calculations may be unphysical. Secondly, in the calculation of the particle trajectories, the turbulence is simulated using a single eddy size, when particles in these flows will actually be influenced by eddies with sizes differing by an order of magnitude. Again, as with turbulence models, these methods for calculating particle trajectories in turbulent flows work well for a narrow range of flows for which they are calibrated (e.g. single particles in homogeneous grid turbulence).

Overcoming these shortcomings may be possible by using more advanced turbulence models such as Large Eddy Simulation (LES) were some of the turbulence is simulated directly. It may then be possible to use some of this information in the particle trajectory calculations to improve their accuracy as well.

In summary, CFD shows promise for calculating the particle deposition in laminar flow, or those flows where turbulent dispersion is not important. However, using current CFD programs with turbulent dispersion can result in serious errors.